

Amplitude analysis and branching fraction measurement of the decay $D_s^+ \rightarrow K^+ \pi^+ \pi^- \pi^0$

BESIII Collaboration



ABSTRACT: The singly Cabibbo-suppressed decay $D_s^+ \rightarrow K^+ \pi^+ \pi^- \pi^0$ is observed by using a data set corresponding to an integrated luminosity of 6.32 fb^{-1} recorded by the BESIII detector at the centre-of-mass energies between 4.178 and 4.226 GeV. The first amplitude analysis of $D_s^+ \rightarrow K^+ \pi^+ \pi^- \pi^0$ reveals the sub-structures in this decay and determines the fractions and relative phases of different intermediate processes. The dominant intermediate process is $D_s^+ \rightarrow K^{*0} \rho^+$, with a fit fraction of $(40.5 \pm 2.8_{\text{stat.}} \pm 1.5_{\text{syst.}})\%$. With the detection efficiency based on our amplitude analysis, the absolute branching fraction for $D_s^+ \rightarrow K^+ \pi^+ \pi^- \pi^0$ is measured to be $(9.75 \pm 0.54_{\text{stat.}} \pm 0.17_{\text{syst.}}) \times 10^{-3}$.

KEYWORDS: Branching fraction, Charm physics, e^+e^- Experiment

Contents

1	Introduction	1
2	Detector and data sets	3
3	Event selection	4
4	Amplitude analysis	6
4.1	Further selection criteria	6
4.2	Fit method	7
4.2.1	Blatt-Weisskopf barrier factors	9
4.2.2	Propagator	9
4.2.3	Spin factors	12
4.3	Fit results	12
4.4	Systematic uncertainties for the amplitude analysis	13
5	Branching fraction measurement	16
6	Summary	20
A	Clebsch-Gordan relation	25
B	Other intermediate processes tested	25

1 Introduction

The hadronic decays of charmed mesons have been studied extensively in both experiment and theory since the discovery of charmed mesons in 1976 by Mark I [1, 2]. However, a precise theoretical description for exclusive hadronic charmed meson decays is still challenging because the mass of charm quark is too light to adopt a sensible heavy quark expansion and too heavy to apply chiral perturbation theory [3]. Amplitude analyses and measurements of the branching fractions (BFs) for hadronic decays of charmed mesons provide valuable information about the underlying mechanism of the charmed meson decays.

Four-body hadronic decays of D_s^+ mesons can be dominated by two-body intermediate processes [4], such as $D_s^+ \rightarrow VV$ and $D_s^+ \rightarrow AP$ decays, where V , A , and P denote vector, axial-vector and pseudoscalar mesons, respectively. The investigations of the $D_s^+ \rightarrow VV$ decays have attracted a great deal of attention [5–9], but the experimental information about the $D_s^+ \rightarrow VV$ decays is sparse. And the improved knowledge of BFs of $D_s^+ \rightarrow AP$ decays, such as $D_s^+ \rightarrow K_1(1270)^0\pi^+$ and $D_s^+ \rightarrow K_1(1400)^0\pi^+$, is important to improve the understanding of the mixing of the $K_1(1270)^0$ and $K_1(1400)^0$ mesons [10]. The singly

Cabibbo-suppressed hadronic decay of $D_s^+ \rightarrow K^+ \pi^+ \pi^- \pi^0$ is expected to be dominated by the intermediate decays $D_s^+ \rightarrow K^{*0} \rho^+$ and $K_1^0 \pi^+$ (ρ denotes $\rho(770)$, K^* denotes $K^*(892)$ and K_1 denotes $K_1(1270)/K_1(1400)$), since the decay width calculated by external W-emission process with final states of neutral kaonic states (i.e. K^{*0} , K_1^0) is greater than internal W-emission process with charged kaonic states (i.e. K^{*+} , K_1^+) and the difference between the annihilation amplitudes could be ignored [11]. Take $D_s^+ \rightarrow K^{*0} \rho^+$ and $K^{*+} \rho^0$ states as an example, the tree T -diagrams and annihilation A -diagrams of these two decay modes are shown in Fig. 1 and Fig. 2, respectively. More experimental information from the amplitude analysis of this decay will offer important experimental input to improve the theory predictions and explore charge-parity (CP) violation in the charm meson decays [9, 12].

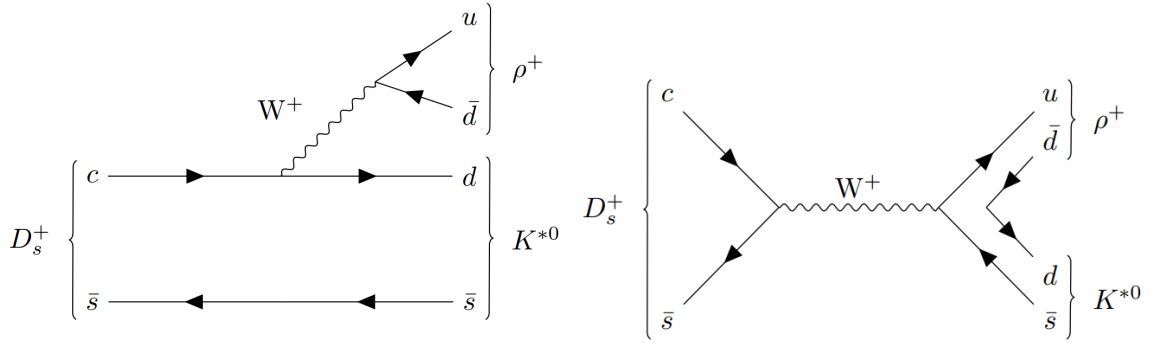


Figure 1. The T -diagrams (left) and A -diagrams (right) for the decay $D_s^+ \rightarrow K^{*0} \rho^+$

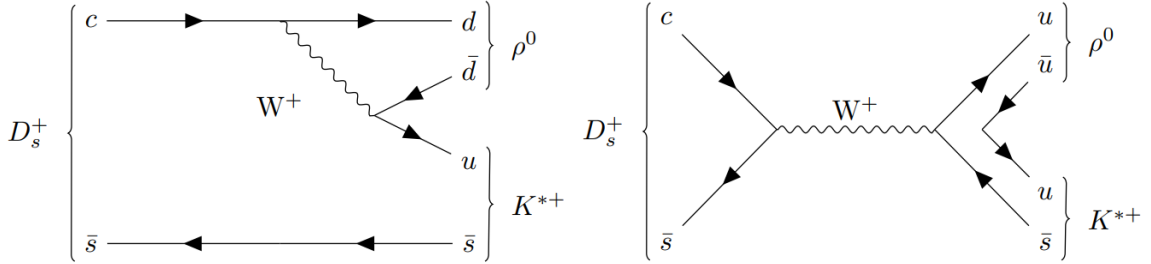


Figure 2. The T -diagrams (left) and A -diagrams (right) for the decay $D_s^+ \rightarrow K^{*+} \rho^0$.

The amplitude analysis of $D_s^+ \rightarrow K^+ \pi^+ \pi^- \pi^0$ also provides access to $D_s^+ \rightarrow VP$ decays, such as $D_s^+ \rightarrow \omega K^+$. Evidence for $D_s^+ \rightarrow \omega K^+$ was first reported by BESIII experiment, and the BF was measured to be $(0.87 \pm 0.25_{\text{stat.}} \pm 0.07_{\text{syst.}}) \times 10^{-3}$ [13], which was based on 3.19 fb^{-1} data samples taken at the center-of-mass energy (E_{cm} or \sqrt{s}) 4.178 GeV. The predicted value of BF (2.12×10^{-3}) [11] was too large compared to the experimental value of (0.87×10^{-3}) , but after taking into account $SU(3)_F$ breaking in internal W-emission, the predicted BF now is reduced to (0.99×10^{-3}) [14]. Therefore, the amplitude of $D_s^+ \rightarrow \omega K^+$ decay is important to investigate the W-annihilation contribution in $D_s^+ \rightarrow VP$ decays and

improve the understanding of $SU(3)_F$ flavor symmetry breaking effects in hadronic decays of charmed mesons [11, 14, 15].

This paper reports the first amplitude analysis and BF measurement of the decay $D_s^+ \rightarrow K^+\pi^+\pi^-\pi^0$, using e^+e^- collision data samples corresponding to an integrated luminosity of 6.32 fb^{-1} collected at the \sqrt{s} between 4.178 and 4.226 GeV with the BESIII detector. Charged-conjugate modes are always implied throughout this paper except when discussing CP violation.

2 Detector and data sets

The BESIII detector is a magnetic spectrometer [16, 17] located at the Beijing Electron Positron Collider (BEPCII) [18]. The cylindrical core of the BESIII detector covers 93% of the full solid angle and consists of a helium-based multilayer drift chamber (MDC), a plastic scintillator time-of-flight system (TOF), and a CsI(Tl) electromagnetic calorimeter (EMC), which are all enclosed in a superconducting solenoidal magnet providing a 1.0 T magnetic field. The solenoid is supported by an octagonal flux-return yoke with resistive plate counter muon identification modules interleaved with steel. The resolution of charged-particle momentum at 1 GeV/ c is 0.5%, and the resolution of specific energy loss dE/dx is 6% for electrons from Bhabha scattering. The EMC measures photon energies with a resolution of 2.5% (5%) at 1 GeV in the barrel (end cap) region. The time resolution in the TOF barrel region is 68 ps, while that in the end cap region is 110 ps. The end cap TOF system was upgraded in 2015 using multi-gap resistive plate chamber technology, providing a time resolution of 60 ps [19–21]. About 83% of the data in this analysis benefits from the upgrade.

The integrated luminosities of different centre-of-mass energies of the data samples used in this analysis are listed in Table 1 [22–24]. For some aspects of the analysis, these samples are organised into three sample groups, 4.178 GeV, 4.189–4.219 GeV, and 4.226 GeV, and each of them is acquired during the same year under consistent running conditions. Since the cross section of $D_s^{*\pm}D_s^\mp$ production in e^+e^- annihilation is about a factor of twenty larger than that of $D_s^+D_s^-$ [25], and the $D_s^{*\pm}$ meson decays to γD_s^\pm have a dominant BF of $(93.5 \pm 0.7)\%$ [4], the signal events discussed in this paper are selected from the process $e^+e^- \rightarrow D_s^{*\pm}D_s^\mp \rightarrow \gamma D_s^+D_s^-$.

Simulated samples produced with a GEANT4-based [26] Monte Carlo (MC) package, which includes the geometric description of the BESIII detector and the detector response, are used to determine detection efficiencies and to estimate backgrounds. The simulation models the beam energy spread and initial state radiation in the e^+e^- annihilations with the generator KKMC [27, 28]. The inclusive MC sample includes the production of open charm processes, the initial state radiation production of vector charmonium(-like) states, and the continuum processes incorporated in KKMC [27, 28]. The known decay modes are modeled with EVTGEN [29, 30] using BFs taken from the Particle Data Group (PDG) [4], and the remaining unknown charmonium decays are modeled with LUNDCHARM [31, 32]. Final state radiation from charged final state particles is incorporated using PHOTOS [33].

\sqrt{s} (GeV)	\mathcal{L}_{int} (pb $^{-1}$)
4.178	3189.0 \pm 0.2 \pm 31.9
4.189	526.7 \pm 0.1 \pm 2.2
4.199	526.0 \pm 0.1 \pm 2.1
4.209	517.1 \pm 0.1 \pm 1.8
4.219	514.6 \pm 0.1 \pm 1.8
4.226	1056.4 \pm 0.1 \pm 7.0

Table 1. The integrated luminosities (\mathcal{L}_{int}) for various centre-of-mass energies. The first and second uncertainties are statistical and systematic, respectively.

3 Event selection

To obtain the signal samples with high purity, we adopt the double tag method [34] in this analysis. In this method, a single-tag (ST) candidate requires only one of the D_s^\pm mesons to be reconstructed via a hadronic decay; a double-tag (DT) candidate has both $D_s^+ D_s^-$ mesons reconstructed via hadronic decays, where one D_s meson is reconstructed via the signal mode and the other via any of the tag modes. The D_s^\pm candidates are constructed from individual π^\pm , π^0 , K^\pm , K_S^0 , η and η' particles, with the following selection criteria.

All charged tracks reconstructed in the MDC must satisfy $|\cos\theta| < 0.93$, where θ is the polar angle of a charged track with respect to the positive direction of the MDC axis. For charged tracks not originating from K_S^0 decays, the distance of closest approach to the interaction point is required to be less than 10 cm along the beam direction and less than 1 cm in the plane perpendicular to the beam. Particle identification (PID) for charged tracks is performed by using the dE/dx measured by the MDC and the flight time in the TOF. The confidence level for pion and kaon hypotheses (CL_K and CL_π) are calculated. Kaon and pion candidates are required to satisfy $CL_K > CL_\pi$ and $CL_\pi > CL_K$, respectively.

The K_S^0 candidates are reconstructed from two oppositely charged tracks. The distances of the charged tracks to the interaction point along the beam direction are required to be less than 20 cm. The two charged tracks are assigned as $\pi^+\pi^-$ without imposing further PID criteria. They are constrained to originate from a common vertex and are required to have an invariant mass in the interval of $|M_{\pi^+\pi^-} - m_{K_S^0}| < 12 \text{ MeV}/c^2$, where $m_{K_S^0}$ is the known K^0 mass [4]. The decay lengths of the K_S^0 candidates are required to be twice greater than its uncertainty.

Photon candidates are identified by their showers in the EMC. The deposited energy of each shower must be more than 25 MeV in the barrel region ($|\cos\theta| < 0.80$) and more than 50 MeV in the end cap region ($0.86 < |\cos\theta| < 0.92$). The minimum opening angle between the position of each shower in the EMC and the closest extrapolated charged track is required to be greater than 10° to exclude the showers originating from tracks. The difference between the EMC time and the event start time is required to be within [0, 700] ns to suppress electronic noises and showers unrelated to the event.

Tag mode	Mass window (GeV/ c^2)
$D_s^- \rightarrow K_S^0 K^-$	[1.948, 1.991]
$D_s^- \rightarrow K^- K^+ \pi^-$	[1.950, 1.986]
$D_s^- \rightarrow K^+ K^- \pi^- \pi^0$	[1.947, 1.982]
$D_s^- \rightarrow K_S^0 K^+ \pi^- \pi^-$	[1.953, 1.983]
$D_s^- \rightarrow \pi^- \eta \gamma \gamma$	[1.930, 2.000]
$D_s^- \rightarrow \pi^- \eta'_{\pi^+\pi^-} \gamma \gamma$	[1.938, 1.997]

Table 2. The M_{tag} requirements for various tag modes, where the subscripts of η and η' denote the decay modes used to reconstruct these particles.

\sqrt{s} (GeV)	M_{rec} (GeV/ c^2)
4.178	[2.050, 2.180]
4.189	[2.048, 2.190]
4.199	[2.046, 2.200]
4.209	[2.044, 2.210]
4.219	[2.042, 2.220]
4.226	[2.040, 2.220]

Table 3. The requirements of M_{rec} for each data set.

The π^0 and η candidates are formed from the photon pairs with invariant masses being in the ranges [0.115, 0.150] GeV/ c^2 and [0.490, 0.580] GeV/ c^2 , respectively, which are about three times of the resolution of the detector. Moreover, at least one of this two photons is required to be from the barrel EMC to achieve better resolution. A kinematic fit that constrains the $\gamma\gamma$ invariant mass to the known π^0 or η mass [4] is performed to improve the reconstructed D_s^\pm mass resolution. The χ^2 of the kinematic fit is required to be less than 30. The η' candidates are formed from $\pi^+\pi^-\eta$ combinations with an invariant mass within the range of [0.946, 0.970] GeV/ c^2 .

Six tag modes are used and combined to select the signals of $D_s^+ \rightarrow K^+\pi^+\pi^-\pi^0$. The corresponding mass windows on the tagged D_s^- mass (M_{tag}) are listed in Table 2. The quantity M_{rec} is defined as

$$M_{\text{rec}} = \sqrt{\left(E_{\text{cm}} - \sqrt{|\vec{p}_{D_s}^2} + m_{D_s}^2}\right)^2 - |\vec{p}_{D_s}^2|}, \quad (3.1)$$

where \vec{p}_{D_s} is the three-momentum of the D_s^- candidate in the e^+e^- centre-of-mass frame, and m_{D_s} is the known D_s mass [4]. Events with both signal and tag D_s candidates having their M_{rec} falling within the bounds listed in Table 3 are retained for further study.

4 Amplitude analysis

4.1 Further selection criteria

To obtain data samples with high purities for the amplitude analysis, the following dedicated selection criteria are imposed on the signal candidates.

The seven-constraint kinematic fit to the process $e^+e^- \rightarrow D_s^{*\pm}D_s^\mp \rightarrow \gamma D_s^+D_s^-$, where the D_s^- decays to one of the tag modes and the D_s^+ decays to the signal mode, is required to converge. In addition to the constraints of four-momentum conservation in the e^+e^- centre-of-mass system, the invariant masses of $(\gamma\gamma)_{\pi^0}$, tag D_s^- , and $D_s^{*\pm}$ candidates are constrained to the corresponding known masses [4]. The combination with the minimum χ^2 is chosen, assuming that D_s^{*+} decays to $D_s^+\gamma$ or D_s^{*-} decays to $D_s^-\gamma$. In order to ensure that all candidates fall within the phase-space boundary, the constraint of the signal D_s^+ mass is added to the kinematic fit and the updated four-momenta from this kinematic fit are used for the amplitude analysis.

A K_S^0 mass veto, $M_{\pi^+\pi^-} \notin [0.460, 0.520]$ GeV/ c^2 , which is about ± 3 times of the K_S^0 resolution, is applied on the signal D_s^+ to remove the dominant background from $D_s^+ \rightarrow K^+K_S^0\pi^0$ ($K_S^0 \rightarrow \pi^+\pi^-$) decays. An η mass veto, $M_{\pi^+\pi^-\pi^0} \notin [0.520, 0.580]$ GeV/ c^2 , which is about ± 3 times the η resolution, is also applied to remove the events from $D_s^+ \rightarrow K^+\eta$ ($\eta \rightarrow \pi^+\pi^-\pi^0$) decays.

The energy of the transition photon from $D_s^{*+} \rightarrow \gamma D_s^+$ is required to be less than 0.18 GeV. The recoiling mass against this photon and the signal D_s^+ candidate is required to lie within the range of [1.955, 1.995] GeV/ c^2 .

There is a wrong-combination background from $D^0 \rightarrow K^-\pi^+\pi^0$ versus $\bar{D}^0 \rightarrow K^+\pi^+\pi^-\pi^-$, which fakes $D_s^+ \rightarrow K^+\pi^+\pi^-\pi^0$ versus $D_s^- \rightarrow K^-K_S^0$, $K_S^0 \rightarrow \pi^+\pi^-$ by exchanging a π^0 and π^- . It also fakes $D_s^+ \rightarrow K^+\pi^+\pi^-\pi^0$ versus $D_s^- \rightarrow K^+K^-\pi^-$ by identifying a π^+ from the D^0 as a K^+ and exchanging a π^- from the \bar{D}^0 with the π^0 from D^0 . This background is excluded by rejecting the events which simultaneously satisfy $|M_{K^-\pi^+\pi^0} - M_{D^0}| < 75$ MeV/ c^2 and $|M_{K^+\pi^+\pi^-\pi^0} - M_{\bar{D}^0}| < 50$ MeV/ c^2 , where M_{D^0} is the known D^0 mass [4]. There is also a wrong-combination background from $D^+ \rightarrow K^+K_S^0K_S^0$, $K_S^0 \rightarrow \pi^+\pi^-$ versus $D^- \rightarrow K^+\pi^-\pi^-$, it fakes $D_s^+ \rightarrow K^+\pi^+\pi^-\pi^0$ versus $D_s^- \rightarrow K_S^0K^+\pi^-\pi^-$ by exchanging π^+ and π^- , then adding a π^0 . This background is excluded by rejecting the events which simultaneously satisfy $|M_{K^+\pi^+\pi^-\pi^0} - M_{D^+}| < 50$ MeV/ c^2 and $|M_{K^+\pi^-\pi^-} - M_{D^-}| < 75$ MeV/ c^2 , where M_{D^+} is the known D^+ mass [4].

Figure 3 shows the fits to the invariant-mass distributions of the accepted signal D_s^+ candidates, M_{sig} , for various data samples. In the fits, the signal is described by a MC-simulated shape convolved with a Gaussian function and the background is described by a simulated shape derived from the inclusive MC sample. Then, a mass window, [1.940, 1.985] GeV/ c^2 , is applied on the signal D_s^+ candidates. Finally, there are 344, 222, and 64 events retained for the amplitude analysis with purities of $(85.1 \pm 1.9)\%$, $(90.0 \pm 2.0)\%$, and $(86.1 \pm 4.3)\%$ for the data samples at $\sqrt{s} = 4.178, 4.189\text{-}4.219, \text{ and } 4.226$ GeV, respectively.

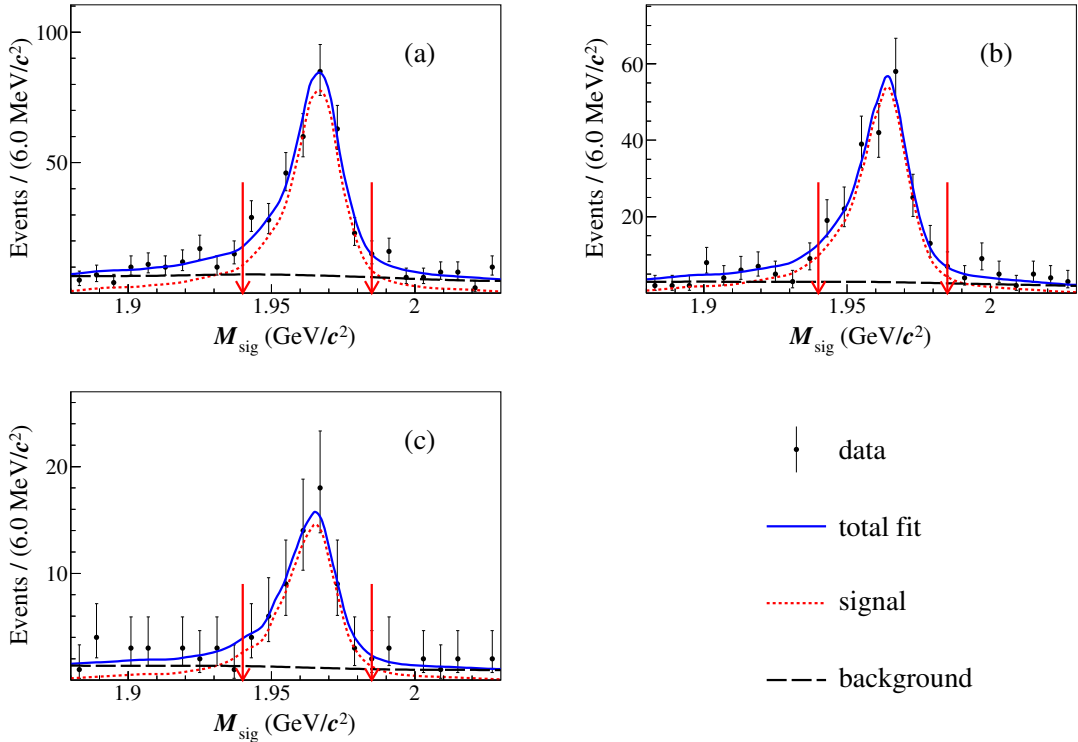


Figure 3. Fits to the M_{sig} distributions of the data samples at $\sqrt{s} =$ (a) 4.178 GeV, (b) 4.189-4.219 GeV and (c) 4.226 GeV. The black points with error bars are data. The blue solid lines are the total fits. The red dotted and black dashed lines are the fitted signal and background, respectively. The pairs of red arrows indicate the signal regions.

4.2 Fit method

An unbinned maximum likelihood fit is used in the amplitude analysis of $D_s^+ \rightarrow K^+\pi^+\pi^-\pi^0$, the likelihood function \mathcal{L} is constructed with a signal-background combined probability density function (PDF), which depends on the momenta of the four final state particles. The likelihood is written as

$$\mathcal{L} = \prod_{i=1}^3 \prod_{k=1}^{N_{D,i}} \left[w^i f_S(p^k) + (1 - w^i) f_B(p^k) \right], \quad (4.1)$$

where i indicates the data sample groups. The p^k denotes the four-momenta of the final state particles, where k denotes the k^{th} event in the data sample i . The $N_{D,i}$ is the number of candidates in the data sample i , f_S (f_B) is the signal (background) PDF and w^i is the purity of the signal discussed in Sec. 4.1.

The signal PDF is given by

$$f_S(p) = \frac{\epsilon(p) |\mathcal{M}(p)|^2 R_4}{\int \epsilon(p) |\mathcal{M}(p)|^2 R_4 dp}, \quad (4.2)$$

where $\epsilon(p)$ is the detection efficiency in bins of a five-dimensional space of two- and three-body invariant masses, and R_4 is the four-body phase space. The total amplitude \mathcal{M} is

modeled with the isobar model, which is the coherent sum of the individual amplitudes of intermediate processes, given by $\mathcal{M} = \sum \rho_n e^{i\phi_n} \mathcal{A}_n$, where the magnitude ρ_n and phase ϕ_n are the free parameters to be determined by the fit. The amplitude of the n^{th} intermediate process (\mathcal{A}_n) is given by

$$\mathcal{A}_n = P_n^1 P_n^2 S_n F_n^1 F_n^2 F_n^3, \quad (4.3)$$

where the indices 1, 2 and 3 correspond to the two subsequent intermediate resonances and the D_s^+ meson. Here F_n is the Blatt-Weisskopf barrier (Sec. 4.2.1), P_n is the propagator of the intermediate resonance (Sec. 4.2.2), and S_n is the spin factor constructed with the covariant tensor formalism [35] (Sec. 4.2.3). The normalisation integral is realised by MC integration,

$$\int \epsilon(p) |\mathcal{M}(p)|^2 R_4 dp \approx \frac{1}{N_{\text{MC}}} \sum_{k=1}^{N_{\text{MC}}} \frac{|\mathcal{M}(p^k)|^2}{|\mathcal{M}^g(p^k)|^2}, \quad (4.4)$$

where k is the index of the k^{th} event of the signal MC sample, and N_{MC} is the number of the selected MC events. The $\mathcal{M}^g(p)$ is the signal PDF used to generate the signal MC sample in the MC integration. The normalization integral for background is also realised by a MC integration method like Eq. 4.4,

$$\int \epsilon(p) B_\epsilon(p) R_4 dp \approx \frac{1}{N_{\text{MC}}} \sum_{k_{\text{MC}}}^{N_{\text{MC}}} \frac{B_\epsilon(p^{k_{\text{MC}}})}{|M^{\text{gen}}(p^{k_{\text{MC}}})|^2}, \quad (4.5)$$

To account for the bias caused by differences in tracking, PID efficiencies and π^0 reconstruction between data and MC simulation, each signal MC event is weighted with a ratio, $\gamma_\epsilon(p)$, and it is calculated as

$$\gamma_\epsilon(p) = \prod_j \frac{\epsilon_{j,\text{data}}(p)}{\epsilon_{j,\text{MC}}(p)}, \quad (4.6)$$

where j denotes the final four daughter particles, $\epsilon_{j,\text{data}}(p)$ and $\epsilon_{j,\text{MC}}(p)$ are the tracking, PID and π^0 reconstruction efficiencies as a function of the momenta of the daughter particles for data and MC simulation, respectively. By weighting each signal MC event with γ_ϵ , the MC integration is modified to be

$$\int \epsilon(p) |\mathcal{M}(p)|^2 R_4 dp \approx \frac{1}{N_{\text{MC}}} \sum_{k=1}^{N_{\text{MC}}} \frac{|\mathcal{M}(p^k)|^2 \gamma_\epsilon(p^{k_{\text{MC}}})}{|\mathcal{M}^g(p^k)|^2}. \quad (4.7)$$

The background PDF is given by

$$f_B(p) = \frac{\epsilon(p) B_\epsilon(p) R_4}{\int \epsilon(p) B_\epsilon(p) R_4 dp}, \quad (4.8)$$

where $B_\epsilon(p) = B(p)/\epsilon(p)$ is the efficiency-corrected background shape. The background shape $B(p)$ is derived by using a multi-dimensional kernel density estimator [36] named RooNDKeysPdf implemented in RooFit [37], which models the distribution of an input

dataset as a superposition of Gaussian kernels using background events in the M_{sig} signal region from the inclusive MC sample. The $M_{K^+\pi^-}$, $M_{K^+\pi^0}$, $M_{\pi^+\pi^-}$, $M_{\pi^+\pi^0}$ and $M_{K^+\pi^-\pi^0}$ distributions of the inclusive MC events outside the M_{sig} signal region are compared to these distributions from the data to check their validity. The distributions of background events from the inclusive MC sample within and outside the M_{sig} signal region are also examined. They are compatible with each other within statistical uncertainties.

4.2.1 Blatt-Weisskopf barrier factors

For the process $a \rightarrow bc$, the Blatt-Weisskopf barrier factors [38], $X_L(p)$, are parameterised as a function of the angular momenta L and the momenta q of the final state particle b or c in the rest system of a . They are taken as

$$\begin{aligned} X_{L=0}(q) &= 1, \\ X_{L=1}(q) &= \sqrt{\frac{z_0^2 + 1}{z^2 + 1}}, \\ X_{L=2}(q) &= \sqrt{\frac{z_0^4 + 3z_0^2 + 9}{z^4 + 3z^2 + 9}}, \end{aligned} \quad (4.9)$$

where $z = qR$, $z_0 = q_0R$ and the effective radius of the barrier R is fixed to 3.0 GeV^{-1} for the intermediate resonances and 5.0 GeV^{-1} for the D_s^+ meson. The momentum q is given by

$$q = \sqrt{\frac{(s_a + s_b - s_c)^2}{4s_a} - s_b}, \quad (4.10)$$

the value of q_0 is that of q when $s_a = m_a^2$ and the $s_a(s_b, s_c)$ denotes the invariant-mass squared of the particle $a(b, c)$.

4.2.2 Propagator

The intermediate resonances K^{*0} , K^{*+} , $K_1(1270)^0$, $K_1(1400)^0$ and $a_1(1260)^0$ are parameterised with the relativistic Breit-Wigner (RBW) function,

$$P(m) = \frac{1}{m_0^2 - s_a - im_0\Gamma(m)}, \quad \Gamma(m) = \Gamma_0 \left(\frac{q}{q_0}\right)^{2L+1} \left(\frac{m_0}{m}\right) \left(\frac{X_L(q)}{X_L(q_0)}\right)^2, \quad (4.11)$$

where m_0 and Γ_0 denote the resonance's rest mass and width. The masses and widths of the intermediate resonances, except for $K_1(1270)^0$, are fixed to the PDG values [4]. Considering the obvious mass deviation reported in the PDG [4], the mass and width of $K_1(1270)^0$ are fixed to $1289 \text{ MeV}/c^2$ and 116 MeV , respectively, from results obtained by the LHCb experiment [39].

The ρ resonances are parameterised by the Gounaris-Sakurai (GS) lineshape [40], which is given by

$$P_{\text{GS}}(m) = \frac{1 + d\frac{\Gamma_0}{m_0}}{m_0^2 - m^2 + f(m) - im_0\Gamma(m)}. \quad (4.12)$$

The function $f(m)$ is given by

$$f(m) = \Gamma_0 \frac{m_0^2}{q_0^3} \left[q^2 (h(m) - h(m_0)) + (m_0^2 - m^2) q_0^2 \frac{dh}{d(m^2)} \Big|_{m_0^2} \right], \quad (4.13)$$

where

$$h(m) = \frac{2q}{\pi m} \ln \left(\frac{m + 2q}{2m_\pi} \right), \quad (4.14)$$

and

$$\frac{dh}{d(m^2)} \Big|_{m_0^2} = h(m_0) [(8q_0^2)^{-1} - (2m_0^2)^{-1}] + (2\pi m_0^2)^{-1}. \quad (4.15)$$

The normalisation condition at $P_{\text{GS}}(0)$ fixes the parameter $d = f(0)/(\Gamma_0 m_0)$ as

$$d = \frac{3m_\pi^2}{\pi q_0^2} \ln \left(\frac{m_0 + 2q_0}{2m_\pi} \right) + \frac{m_0}{2\pi q_0} - \frac{m_\pi^2 m_0}{\pi q_0^3}. \quad (4.16)$$

The K -Matrix parametrisation is used to describe the $\pi^+\pi^-$ S-wave. Detailed descriptions of the K -matrix formalism can be found in various references [41–44]; parameters used are summarised in Tables 4 and 5. We use the “ K -matrix amplitude” to describe the amplitude of channel u ($u = 1 - 5$ denote the channels $\pi\pi, K\bar{K}, 4\pi, \eta\eta, \eta\eta'$) in the form of $A_u = (I - i\hat{K}\rho)_{uv}^{-1} \hat{P}_v$. Here the vector \hat{P} describes the production of bare states and the non-resonant production of meson pairs, while the term $(I - i\hat{K}\rho)^{-1}$ describes their re-scattering.

Table 4. K -matrix parameters from a global analysis of the available $\pi\pi$ scattering data from threshold up to 1900 MeV/ c^2 . Masses and coupling constants are given in GeV/ c^2

α	m_α	$g_{\pi^+\pi^-}^\alpha$	$g_{K\bar{K}}^\alpha$	$g_{4\pi}^\alpha$	$g_{\eta\eta}^\alpha$	$g_{\eta\eta'}^\alpha$
1	0.65100	0.22889	-0.55377	0.00000	-0.398994	-0.34639
2	1.20360	0.94128	0.55095	0.00000	0.39065	0.31503
3	1.55817	0.36856	0.23888	0.55639	0.18340	0.18681
4	1.21000	0.33650	0.40907	0.85679	0.19906	-0.00984
5	1.82206	0.18171	-0.17558	-0.79658	-0.00355	0.22358
s_0^{sacct}	f_{11}^{sacct}	f_{12}^{sacct}	f_{13}^{sacct}	f_{14}^{sacct}	f_{15}^{sacct}	
-3.92637	0.23399	0.15044	-0.20545	0.32825	0.35412	
s_{A0}	s_A	s_0^{prod}				
-0.15	1.0	-3.0 ± 0.03				

The scattering matrix \hat{K} can be parameterised as a combination of the sum of N poles with real bare masses m_α , together with slowly-varying non-resonant parts (SVPs):

$$\hat{K}_{uv}(s) = \left(\sum_{\alpha=1}^{N_{\text{poles}}} \frac{g_u^\alpha g_v^\alpha}{m_\alpha^2 - s} + f_{uv}^{\text{sacct}} \frac{m_0^2 - s_0^{\text{sacct}}}{s - s_0^{\text{sacct}}} \right) \left[\frac{1 \text{ GeV}^2/c^4 - s_{A0}}{s - s_{A0}} (s - s_A m_\pi^2/2) \right], \quad (4.17)$$

Table 5. $\pi\pi$ S-wave P-vector parameters obtained from the $D^0 \rightarrow K_S^0 \pi^+ \pi^-$ Dalitz plot distribution from $D^{*+} \rightarrow D^0 \pi^+$. P-vector parameters $f_{1v}^{\prime prod}$, for $v \neq 1$, are defined as $f_{1v}^{prod}/f_{11}^{prod}$.

Component	a_r	$\phi_r(\text{deg})$
β_1	9.3 ± 0.4	-78.7 ± 1.6
β_2	10.89 ± 0.26	-159.1 ± 2.6
β_3	24.2 ± 2.0	168.0 ± 4.0
β_4	9.16 ± 0.24	90.5 ± 2.6
f_{11}^{prod}	7.94 ± 0.26	73.9 ± 1.1
$f_{12}^{\prime prod}$	2.0 ± 0.3	-18.0 ± 9
$f_{13}^{\prime prod}$	5.1 ± 0.3	33 ± 3
$f_{14}^{\prime prod}$	3.23 ± 0.18	4.8 ± 2.5

where g_u^α denotes the real coupling constant of the pole m_α to the meson channel u . The parameters f_{uv}^{scatt} and s_0^{scatt} describe a smooth part for the K -matrix elements and m_0^2 , s_A , and s_{A_0} are real constants of order unity. All these parameters are taken from Ref. [42]. Here s denotes the invariant mass squared of $\pi^+ \pi^-$.

The production vector \hat{P} vector is parameterised in a form analogous to the \hat{K} matrix and it is given by

$$\hat{P}_v(s) = f_v^{\text{prod}} \frac{1 - s_0^{\text{prod}}}{s - s_0^{\text{prod}}} + \sum_{\alpha} \frac{\beta_{\alpha} g_v^{\alpha}}{m_{\alpha}^2 - s}, \quad (4.18)$$

where β_{α} and f_v^{prod} are complex production constants for the poles and non-resonant SVPs, respectively, both of them depend on the final state channel.

The $K\pi$ S-wave is modeled by a parameterisation from scattering data [45], which is described by a $K_0^*(1430)$ Breit-Wigner together with an effective range non-resonant component with a phase shift. It is given by

$$A(m) = F \sin \delta_F e^{i\delta_F} + R \sin \delta_R e^{i\delta_R} e^{i2\delta_F}, \quad (4.19)$$

with

$$\begin{aligned} \delta_F &= \phi_F + \cot^{-1} \left[\frac{1}{aq} + \frac{rq}{2} \right], \\ \delta_R &= \phi_R + \tan^{-1} \left[\frac{M\Gamma(m_{K\pi})}{M^2 - m_{K\pi}^2} \right], \end{aligned} \quad (4.20)$$

where the parameters $F(\phi_F)$ and $R(\phi_R)$ are the magnitude (phase) for non-resonant state and resonance terms, respectively. The parameters a and r are the scattering length and effective interaction length, respectively. We fix these parameters ($M, \Gamma, F, \phi_F, R, \phi_R, a, r$) to the results obtained from the amplitude analysis to a sample of $D^0 \rightarrow K_S^0 \pi^+ \pi^-$ by the BABAR and Belle experiments [45]; these parameters are summarised in Table 6.

M (GeV/ c^2)	1.441 ± 0.002
Γ (GeV)	0.193 ± 0.004
F	0.96 ± 0.07
ϕ_F ($^\circ$)	0.1 ± 0.3
R	1 (fixed)
ϕ_R ($^\circ$)	-109.7 ± 2.6
a (GeV/ c) $^{-1}$	0.113 ± 0.006
r (GeV/ c) $^{-1}$	-33.8 ± 1.8

Table 6. The $K\pi$ S-wave parameters, obtained from the amplitude analysis of $D^0 \rightarrow K_S^0 \pi^+ \pi^-$ by the BABAR and Belle experiments [45]. The uncertainties are combined from the statistical and systematic uncertainties.

4.2.3 Spin factors

For the process $a \rightarrow bc$, the four-momenta of the particles a , b , and c are denoted as p_a , p_b , and p_c , respectively. The spin projection operators [35] are defined as

$$\begin{aligned}
P^{(0)}(a) &= 1, \\
P_{\mu\mu'}^{(1)}(a) &= -g_{\mu\mu'} + \frac{p_{a,\mu} p_{a,\mu'}}{p_a^2}, \\
P_{\mu\nu\mu'\nu'}^{(2)}(a) &= \frac{1}{2} \left(P_{\mu\mu'}^{(1)}(a) P_{\nu\nu'}^{(1)}(a) + P_{\mu\nu'}^{(1)}(a) P_{\nu\mu'}^{(1)}(a) \right) \\
&\quad - \frac{1}{3} P_{\mu\nu}^{(1)}(a) P_{\mu'\nu'}^{(1)}(a).
\end{aligned} \tag{4.21}$$

The pure orbital angular-momentum covariant tensors are given by

$$\begin{aligned}
\tilde{t}_\mu^{(0)}(a) &= 1, \\
\tilde{t}_\mu^{(1)}(a) &= -P_{\mu\mu'}^{(1)}(a) r_a^{\mu'}, \\
\tilde{t}_{\mu\nu}^{(2)}(a) &= P_{\mu\nu\mu'\nu'}^{(2)}(a) r_a^{\mu'} r_a^{\nu'},
\end{aligned} \tag{4.22}$$

where $r_a = p_b - p_c$. The spin factors $S(p)$ used are listed in Table 7. The tensor describing the D_s^+ decays with orbital angular-momentum quantum number l is denoted by $\tilde{T}^{(l)\mu}$ and that of intermediate $a \rightarrow bc$ decay is denoted by $\tilde{t}^{(l)\mu}$, and the $\tilde{T}^{(l)\mu}$ has the same definition as $\tilde{t}^{(l)\mu}$ in Ref. [35].

4.3 Fit results

Using the method described in Sec. 4.2, we perform an unbinned maximum likelihood fit to the $D_s^+ \rightarrow K^+ \pi^+ \pi^- \pi^0$ decay channel. The fit is performed in steps, by adding resonances one by one. The corresponding statistical significance for the newly added amplitude is calculated with the change of the log likelihood value, taking the change of the number of the degrees of freedom into account.

For the amplitude fits, the magnitude and phase of the $D_s^+ \rightarrow K^{*0} \rho^+$ reference amplitude are fixed to 1 and 0, respectively, while those of the other amplitudes are

Decay chain	$S(p)$
$D_s^+[S] \rightarrow V_1 V_2$	$\tilde{t}^{(1)\mu}(V_1) \tilde{t}_\mu^{(1)}(V_2)$
$D_s^+[P] \rightarrow V_1 V_2$	$\epsilon_{\mu\nu\lambda\sigma} p^\mu(D_s^+) \tilde{T}^{(1)\nu}(D_s^+) \tilde{t}^{(1)\lambda}(V_1) \tilde{t}^{(1)\sigma}(V_2)$
$D_s^+ \rightarrow AP_1, A[S] \rightarrow VP_2$	$\tilde{T}^{(1)\mu}(D_s^+) P_{\mu\nu}^{(1)}(A) \tilde{t}^{(1)\nu}(V)$
$D_s^+ \rightarrow V_1 P_1, V_1 \rightarrow V_2 P_2$	$\epsilon_{\mu\nu\lambda\sigma} p_{V_1}^\mu r_{V_1}^\nu p_{P_1}^\lambda r_{V_2}^\sigma$
$D_s^+ \rightarrow SS$	1

Table 7. The spin factors $S(p)$ for various components. All operators, i.e. \tilde{t} and \tilde{T} , have the same definitions as in Ref. [35]. Scalar, pseudo-scalar, vector and axial-vector states are denoted by S , P , V and A , respectively. The $[S]$ and $[P]$ denote the orbital angular-momentum quantum numbers $L = 0$ and 1, respectively.

floated in the fit. The amplitudes for $D_s^+ \rightarrow K^{*+} \rho^0$ and $D_s^+ \rightarrow K^+ \omega$ are also included, as they are clearly observed in the corresponding invariant mass spectra. After testing each, $D_s^+ \rightarrow K_1(1270)^0 \pi^+$ ($K_1(1270)^0 \rightarrow K^+ \rho^-$), $D_s^+ \rightarrow K_1(1400)^0 \pi^+$ ($K_1(1400)^0 \rightarrow K^{*\pm} \pi^\mp$), $D_s^+ \rightarrow K^+ a_1(1260)^0$ ($a_1(1260)^0 \rightarrow \rho^\pm \pi^\mp$), $D_s^+ \rightarrow (K^+ \pi^0)_V \rho^0$, and $D_s^+ \rightarrow (K^+ \pi^0)_{S\text{-wave}} (\pi^+ \pi^-)_{S\text{-wave}}$ are added since each has a statistical significance greater than 3σ . Considering the isospin relationship in hadron decays, some Clebsch-Gordan relations are fixed, with details in Appendix A. A full list of other allowed contributions (based on known states) with statistical significances less than 3σ are listed in Appendix B.

The fit fraction (FF) for the n^{th} amplitude is computed numerically with generator-level MC events with the definition as

$$\text{FF}_n = \frac{\sum_{k=1}^{N_{\text{gen}}} |c_n \mathcal{A}_n^k|^2}{\sum_{k=1}^{N_{\text{gen}}} |\mathcal{M}^k|^2}, \quad (4.23)$$

where N_{gen} is the number of phase space MC signal events at generator level. The sum of these FFs is generally not unity due to net constructive or destructive interference. Interference IN between the n^{th} and n'^{th} amplitudes is defined as

$$\text{IN}_{nn'} = \frac{\sum_{k=1}^{N_{\text{gen}}} 2\text{Re}[c_n c_{n'}^* \mathcal{A}_n^k \mathcal{A}_{n'}^{k*}]}{\sum_{k=1}^{N_{\text{gen}}} |\mathcal{M}^k|^2}. \quad (4.24)$$

In order to determine the statistical uncertainties of FFs, the amplitude coefficients are randomly selected by a Gaussian-distributed set by the fit results according to their uncertainties and the covariance matrix. The distribution of each FF is fitted with a Gaussian function whose width is then taken as the uncertainty of this FF.

The phases, FFs, and statistical significances (Stat.Signi) for different amplitudes are listed in Table 8. The mass projections of the nominal fit are shown in Fig. 4.

4.4 Systematic uncertainties for the amplitude analysis

The systematic uncertainties for the amplitude analysis, summarised in Table 9, are now detailed.

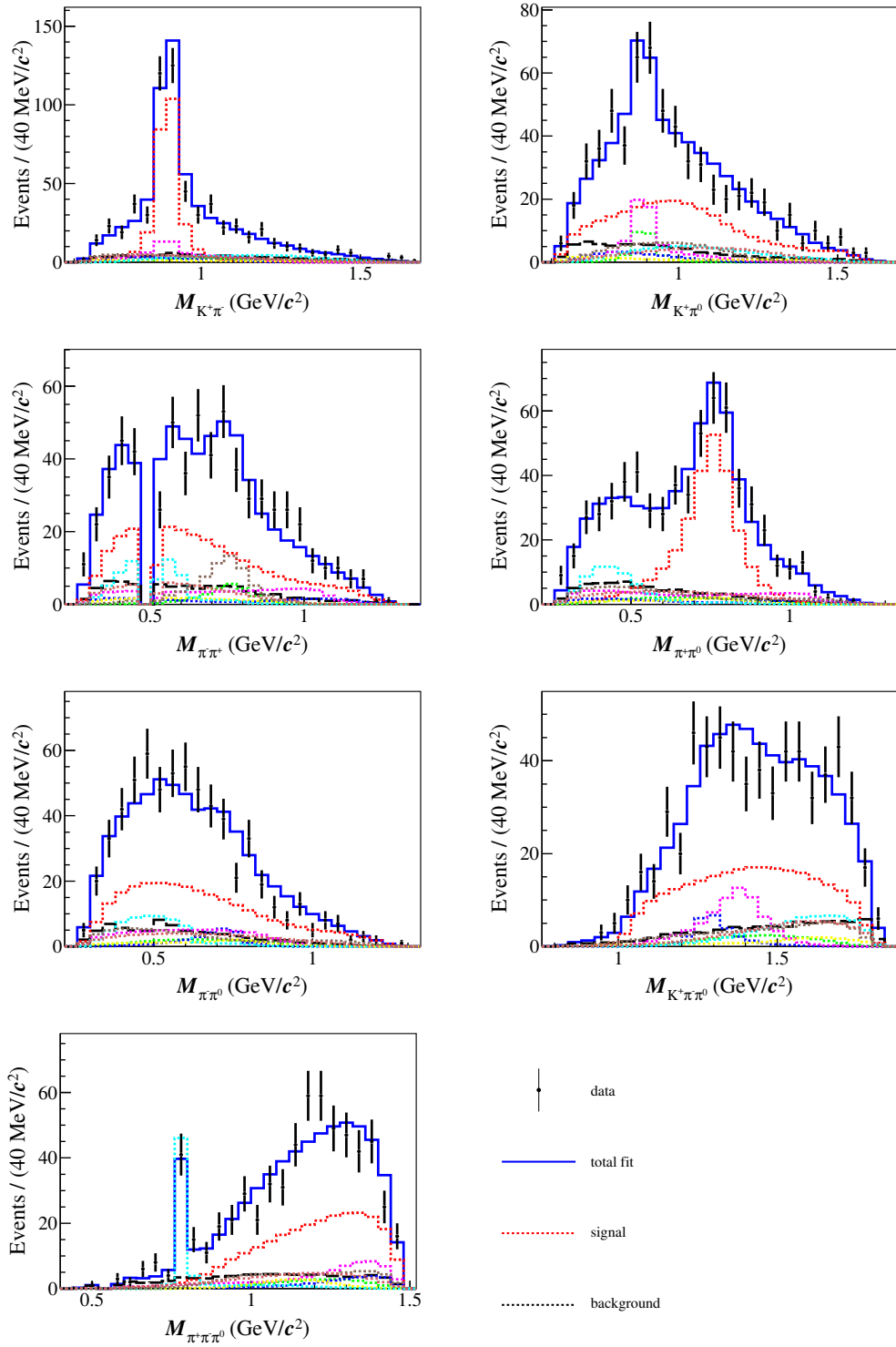


Figure 4. Selected mass projections of the nominal fit. The data samples at $\sqrt{s} = 4.178\text{--}4.226$ GeV are represented by points with error bars, the fit results by the solid blue lines, and the background estimated from the inclusive MC sample by the black dashed lines. Coloured curves show different components of the nominal fit. The total fit is not necessarily equal to the sum of the components due to interference effects.

Amplitude	Phase (rad)	FF (%)	Stat.Signi (σ)
$D_s^+[S] \rightarrow K^{*0}\rho^+$	0.0 (fixed)	$14.5 \pm 2.2 \pm 0.6$	>10
$D_s^+[P] \rightarrow K^{*0}\rho^+$	$2.09 \pm 0.12 \pm 0.03$	$26.0 \pm 2.5 \pm 1.1$	>10
$D_s^+ \rightarrow K^{*0}\rho^+$	-	$40.5 \pm 2.8 \pm 1.5$	>10
$D_s^+[P] \rightarrow K^{*+}\rho^0$	$2.42 \pm 0.21 \pm 0.04$	$4.3 \pm 1.1 \pm 0.6$	6.8
$D_s^+ \rightarrow K^+\omega$	$0.57 \pm 0.23 \pm 0.10$	$9.7 \pm 1.5 \pm 0.6$	>10
$D_s^+ \rightarrow K_1(1270)^0(K^+\rho^-)[S]\pi^+$	$1.80 \pm 0.24 \pm 0.08$	$4.0 \pm 1.2 \pm 0.6$	5.5
$D_s^+ \rightarrow K_1(1400)^0(K^{*+}\pi^-)[S]\pi^+$	$-1.61 \pm 0.17 \pm 0.05$	$5.6 \pm 0.9 \pm 0.2$	-
$D_s^+ \rightarrow K_1(1400)^0(K^{*0}\pi^0)[S]\pi^+$	$-1.61 \pm 0.17 \pm 0.05$	$6.1 \pm 0.9 \pm 0.2$	-
$D_s^+ \rightarrow K_1(1400)^0(K^*\pi)[S]\pi^+$	-	$11.3 \pm 1.8 \pm 0.4$	8.9
$D_s^+ \rightarrow K^+a_1(1260)^0(\rho^+\pi^-)[S]$	$-1.19 \pm 0.25 \pm 0.22$	$1.9 \pm 0.7 \pm 0.9$	-
$D_s^+ \rightarrow K^+a_1(1260)^0(\rho^-\pi^+)[S]$	$-1.19 \pm 0.25 \pm 0.22$	$1.9 \pm 0.7 \pm 0.9$	-
$D_s^+ \rightarrow K^+a_1(1260)^0(\rho\pi)[S]$	-	$3.3 \pm 1.2 \pm 1.5$	3.8
$D_s^+[S] \rightarrow (K^+\pi^0)_V\rho^0$	$1.02 \pm 0.16 \pm 0.08$	$10.4 \pm 2.0 \pm 0.6$	6.6
$D_s^+ \rightarrow (K^+\pi^0)_{S\text{-wave}}(\pi^+\pi^-)_{S\text{-wave}}$	$-2.87 \pm 0.17 \pm 0.06$	$9.5 \pm 2.2 \pm 0.9$	6.0

Table 8. Phases, FFs, and statistical significances for different amplitudes. Groups of related amplitudes are separated by horizontal lines. The last row of each group gives the total fit fraction of the above components with interferences considered. The amplitudes $K_1(1400)^0$ and $a_1(1260)^0$ are constructed by two sub-amplitudes with fixed relations (see Appendix B). The $K^{*0(+)}$ resonance decays to $K^+\pi^{-(0)}$. The $\rho^{+(0)}$ resonance decays to $\pi^+\pi^{0(-)}$. The ω resonance decays to $\pi^+\pi^-\pi^0$. Note that K^* indicates K^{*+} and K^{*0} , ρ indicates ρ^+ and ρ^0 . The first and second uncertainties in the phases and FFs are statistical and systematic, respectively. The total FF is 93.9%.

i Amplitude model:

The masses and widths of resonances are varied by their corresponding uncertainties [4, 39]. The GS lineshape of ρ is replaced with the RBW formula. The coupling constants of the $\pi\pi$ S-wave model are varied within their uncertainties given in Ref. [44]. The changes of the phases and FFs are assigned as the associated systematic uncertainties. Since replacing the lineshape of the $K\pi$ S-wave model from BABAR with the K -matrix formula [46] results in different normalisation factors, the effect on the phase of the amplitude related to $K\pi$ S-wave is not considered for this source.

ii R values:

We assume the distribution of values for barrier effective radius (R), as defined in Sec. 4.2.1, as a uniform distribution. The systematic uncertainties associated with R are estimated by repeating the fit procedure by varying the R of both the intermediate state and D_s^+ mesons by $R/\sqrt{12} \approx 1 \text{ GeV}^{-1}$.

iii Background:

The uncertainty from background size is studied by varying the fractions of signal (equivalent to the fractions of background), i.e. w^i in Eq. 4.1, within their corresponding statistical uncertainties. Another source is the simulation of background shapes. First, alternative MC shapes where the relative fractions of the dominant backgrounds from $e^+e^- \rightarrow q\bar{q}$ ($q = u, d, s$) and non- $D_s^{*\pm}D_s^\mp$ open charm processes are varied by the statistical uncertainties of their cross sections are used. Second,

the background PDF is extracted using other five variable input combinations with varied smoothing parameters of RooNDKeysPDF [37].

iv Simulation effects:

To estimate the uncertainties caused by γ_ϵ , as defined in Eq. 4.6, an amplitude fit is performed by varying efficiencies of PID, tracking and π^0 reconstruction according to their uncertainties.

v Fit bias:

The uncertainty from the fit process is evaluated by studying 600 signal MC samples with the size equal to the data sample size that are generated to check the pull. The pull variables, $(V_{\text{input}} - V_{\text{fit}})/\sigma_{\text{fit}}$, are defined to evaluate the corresponding uncertainty, where V_{input} is the input value in the generator, V_{fit} and σ_{fit} are the output value and the corresponding statistical uncertainty, respectively. Expected to be the standard normal distribution for an unbiased fit, the distributions of pull values for the 600 sets of sample are fitted with a Gaussian function. The fitted mean values for the pulls of FFs of $D_s^+[P] \rightarrow K^{*0}\rho^+$ and $D_s^+ \rightarrow (K^+\pi^0)_{S\text{-wave}}(\pi^+\pi^-)_{S\text{-wave}}$ deviate from zero by larger than 3 times of the standard deviation. We correct all resonances' FFs and phases by the fitted mean values, and assign the uncertainty of the fitted mean values as the corresponding systematic uncertainties.

5 Branching fraction measurement

On top of the selection criteria described in Sec. 3, the momenta of all pions are further required to be greater than 100 MeV/ c to exclude soft pions from D^* decays. The best tag candidate is chosen with M_{rec} closest to m_{D_s} if there are multiple ST candidates. The yields for various tag modes are obtained from the fits to the corresponding M_{tag} distributions and the results are summarised in Table 10. As an example, the fits to the data sample at $\sqrt{s} = 4.178$ GeV are shown in Fig. 5. In the fits, the signal is modeled by an MC-simulated shape convolved with a Gaussian function to take into account the data-MC resolution difference. The background is described by a second-order Chebychev polynomial. Inclusive MC studies show that there is no significant peaking background in any tag mode, except for $D^- \rightarrow K_S^0\pi^-$ and $D_s^- \rightarrow \eta\pi^+\pi^-\pi^-$ faking the $D_s^- \rightarrow K_S^0K^-$ and $D_s^- \rightarrow \pi^-\eta'$ tags, respectively. Therefore, the MC-simulated shapes of these two peaking background sources, with the yields included as free parameters, are added to the fits, respectively.

Once a tag mode is identified, we select the signal decay $D_s^+ \rightarrow K^+\pi^+\pi^-\pi^0$. In the case of multiple candidates, the DT candidate with the average mass, $(M_{\text{sig}} + M_{\text{tag}})/2$, closest to m_{D_s} is retained.

For a given single tag mode, the ST and DT yields can be written as:

$$N_{\text{tag}}^{\text{ST}} = 2N_{D_s^+D_s^-} \mathcal{B}_{\text{tag}} \epsilon_{\text{tag}}^{\text{ST}}, \quad (5.1)$$

$$N_{\text{tag,sig}}^{\text{DT}} = 2N_{D_s^+D_s^-} \mathcal{B}_{\text{tag}} \mathcal{B}_{\text{sig}} \epsilon_{\text{tag,sig}}^{\text{DT}}, \quad (5.2)$$

Amplitude		Source					Total
		i	ii	iii	iv	v	
$D_s^+[S] \rightarrow K^{*0}\rho^+$	FF	0.09	0.10	0.19	0.01	0.06	0.25
$D_s^+[P] \rightarrow K^{*0}\rho^+$	ϕ	0.20	0.02	0.07	0.01	0.06	0.24
	FF	0.10	0.08	0.40	0.03	0.06	0.44
$D_s^+ \rightarrow K^{*0}\rho^+$	FF	0.14	0.02	0.50	0.02	0.06	0.53
$D_s^+[P] \rightarrow K^{*+}\rho^0$	ϕ	0.08	0.04	0.11	0.01	0.05	0.16
	FF	0.15	0.32	0.39	0.01	0.06	0.54
$D_s^+ \rightarrow K^+\omega$	ϕ	0.38	0.11	0.13	0.01	0.05	0.42
	FF	0.09	0.19	0.31	0.01	0.06	0.38
$D_s^+ \rightarrow K_1(1270)^0(K^+\rho^-)[S]\pi^+$	ϕ	0.23	0.11	0.17	0.01	0.06	0.32
	FF	0.13	0.05	0.41	0.01	0.06	0.46
$D_s^+ \rightarrow K_1(1400)^0(K^{*+}\pi^-)[S]\pi^+$	ϕ	0.24	0.08	0.21	0.01	0.06	0.34
	FF	0.18	0.08	0.13	0.01	0.06	0.24
$D_s^+ \rightarrow K_1(1400)^0(K^{*0}\pi^0)[S]\pi^+$	ϕ	0.24	0.08	0.21	0.01	0.06	0.34
	FF	0.20	0.06	0.13	0.02	0.06	0.25
$D_s^+ \rightarrow K_1(1400)^0(K^*\pi)[S]\pi^+$	FF	0.16	0.09	0.12	0.01	0.06	0.23
$D_s^+ \rightarrow K^+a_1(1260)^0(\rho^+\pi^-)[S]$	ϕ	0.83	0.16	0.19	0.01	0.06	0.87
	FF	0.79	0.19	1.01	0.01	0.06	1.31
$D_s^+ \rightarrow K^+a_1(1260)^0(\rho^-\pi^+)[S]$	ϕ	0.83	0.16	0.19	0.01	0.06	0.87
	FF	0.79	0.19	1.01	0.01	0.06	1.31
$D_s^+ \rightarrow K^+a_1(1260)^0(\rho\pi)[S]$	FF	0.77	0.16	1.00	0.02	0.06	1.28
$D_s^+[S] \rightarrow (K^+\pi^0)_V\rho^0$	ϕ	0.08	0.02	0.51	0.02	0.06	0.53
	FF	0.15	0.19	0.13	0.05	0.06	0.30
$D_s^+ \rightarrow (K^+\pi^0)_{S\text{-wave}}(\pi^+\pi^-)_{S\text{-wave}}$	ϕ	0.24	0.21	0.04	0.01	0.04	0.33
	FF	0.14	0.05	0.35	0.01	0.07	0.40

Table 9. Systematic uncertainties on the phases and FFs for different amplitudes in units of the corresponding statistical uncertainties. (i) Amplitude model, (ii) Effective radius, (iii) Background, (iv) Experimental effects, (v) Fit bias.

Tag mode	$N_{\text{ST}}(\text{I})$	$N_{\text{ST}}(\text{II})$	$N_{\text{ST}}(\text{III})$
$D_s^- \rightarrow K_S^0 K^-$	31941 ± 312	18559 ± 261	6582 ± 160
$D_s^- \rightarrow K^+ K^- \pi^-$	137240 ± 614	81286 ± 505	28439 ± 327
$D_s^- \rightarrow K^+ K^- \pi^- \pi^0$	39306 ± 799	23311 ± 659	7785 ± 453
$D_s^- \rightarrow K_S^0 K^+ \pi^- \pi^-$	15719 ± 289	8948 ± 231	3263 ± 172
$D_s^- \rightarrow \pi^- \eta \gamma \gamma$	17940 ± 402	10025 ± 339	3725 ± 252
$D_s^- \rightarrow \pi^- \eta'_{\pi^+\pi^-} \eta \gamma \gamma$	7759 ± 141	4428 ± 111	1648 ± 74

Table 10. The ST yields for the data samples collected at $\sqrt{s} = (\text{I}) 4.178$ GeV, $(\text{II}) 4.189\text{-}4.219$ GeV, and $(\text{III}) 4.226$ GeV. The uncertainties are statistical.

where $N_{D_s^+ D_s^-}$ is the total number of $D_s^{*\pm} D_s^\mp$ pairs produced in the data samples, $N_{\text{tag}}^{\text{ST}}$ is the ST yield for the tag mode; $N_{\text{tag,sig}}^{\text{DT}}$ is the DT yield; \mathcal{B}_{tag} and \mathcal{B}_{sig} are the BF's of the tag and signal modes, respectively; $\epsilon_{\text{tag}}^{\text{ST}}$ is the ST efficiency to reconstruct the tag mode; and $\epsilon_{\text{tag,sig}}^{\text{DT}}$ is the DT efficiency to reconstruct both the tag and signal modes. Summing over

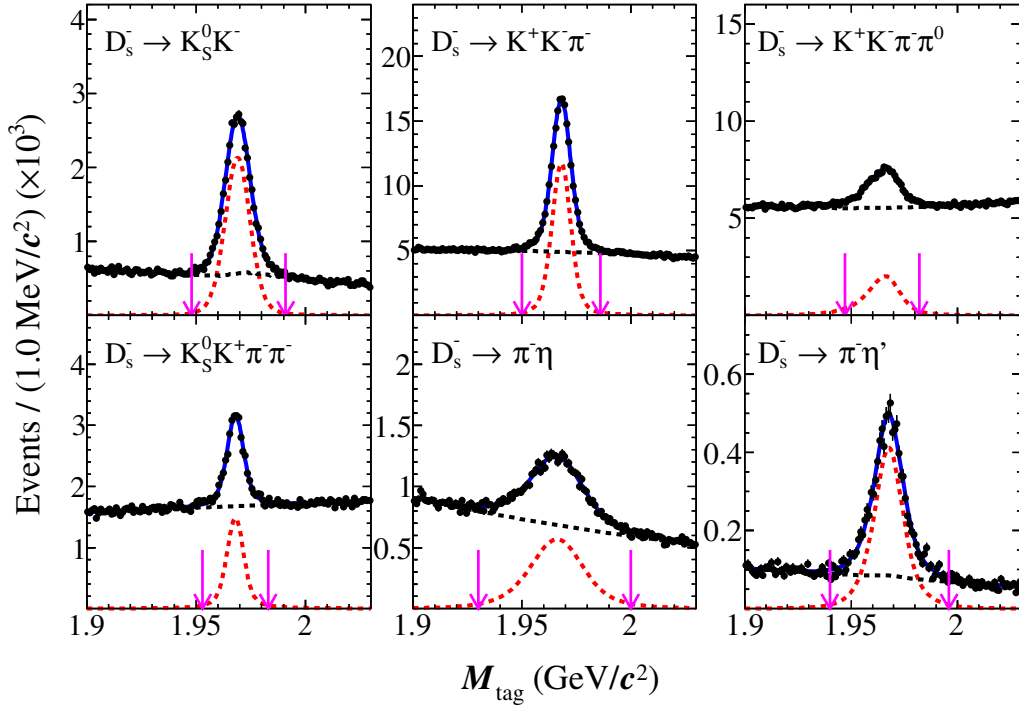


Figure 5. Fits to the M_{tag} distributions of the ST candidates from the data sample at $\sqrt{s} = 4.178$ GeV. The points with error bars are data, the blue solid lines are the total fits, and the black dashed lines are the fitted background. The pairs of red arrows denote the signal regions.

tag modes and sample groups gives the total DT yield:

$$N_{\text{total}}^{\text{DT}} = \sum_{\alpha,i} N_{\alpha,\text{sig},i}^{\text{DT}} = \mathcal{B}_{\text{sig}} \sum_{\alpha,i} 2N_{D_s^+ D_s^-}^i \mathcal{B}_{\alpha} \epsilon_{\alpha,\text{sig},i}^{\text{DT}}, \quad (5.3)$$

where α represents tag modes in the i^{th} sample group. Therefore, the BF of the signal decay can be determined by

$$\mathcal{B}_{\text{sig}} = \frac{N_{\text{total}}^{\text{DT}}}{\mathcal{B}_{\pi^0 \rightarrow \gamma\gamma} \sum_{\alpha,i} N_{\alpha,i}^{\text{ST}} \epsilon_{\alpha,\text{sig},i}^{\text{DT}} / \epsilon_{\alpha,i}^{\text{ST}}}, \quad (5.4)$$

where $N_{\alpha,i}^{\text{ST}}$ and $\epsilon_{\alpha,i}^{\text{ST}}$ are obtained from the data and inclusive MC samples, respectively, while $\epsilon_{\alpha,\text{sig},i}^{\text{DT}}$ is determined with signal MC samples generated based on our amplitude analysis. The branching ratio $\mathcal{B}_{\pi^0 \rightarrow \gamma\gamma}$ has been introduced as it is not included in the MC generation.

The DT yield $N_{\text{total}}^{\text{DT}}$ is found to be 776 ± 43 from the fit to the M_{sig} distribution of the selected $D_s^+ \rightarrow K^+ \pi^+ \pi^- \pi^0$ candidates. The fit result is shown in Fig. 6, where the signal shape is modeled by an MC-simulated shape convolved with a Gaussian function to take into account the data-MC resolution difference. The background shape is derived from the inclusive MC sample. After correcting for the differences in K^+ and π^{\pm} tracking, PID and π^0 reconstruction efficiencies between data and MC simulation, we determine the BF of $D_s^+ \rightarrow K^+ \pi^+ \pi^- \pi^0$ to be $(9.75 \pm 0.54_{\text{stat.}} \pm 0.17_{\text{sys.}}) \times 10^{-3}$ according to Eq. 5.4.

The BFs for the charge-conjugated modes $D_s^+ \rightarrow K^+\pi^+\pi^-\pi^0$ and $D_s^- \rightarrow K^-\pi^-\pi^+\pi^0$, which are labeled as $\mathcal{B}(D_s^+)$ and $\mathcal{B}(D_s^-)$, are measured to be $(9.10 \pm 0.71_{\text{stat.}} \pm 0.16_{\text{syst.}}) \times 10^{-3}$ and $(10.39 \pm 0.79_{\text{stat.}} \pm 0.18_{\text{syst.}}) \times 10^{-3}$, respectively. The asymmetry of the BFs, $A_{CP} = \frac{\mathcal{B}(D_s^+) - \mathcal{B}(D_s^-)}{\mathcal{B}(D_s^+) + \mathcal{B}(D_s^-)}$, is determined to be $(6.5 \pm 5.4_{\text{stat.}} \pm 0.7_{\text{syst.}})\%$. No significant CP violation is observed with the current sample size. Note that the systematic uncertainties due to pion tracking and PID, π^0 reconstruction are canceled in the A_{CP} calculation.

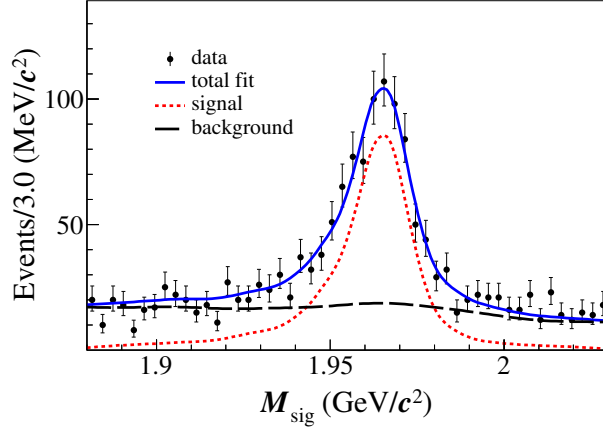


Figure 6. Fit to the M_{sig} distribution of the DT candidates from the data samples at $\sqrt{s} = 4.178\text{--}4.226$ GeV. The data are represented by points with error bars, the total fit by the blue solid line, and the fitted signal and background by the red dotted and black dashed lines, respectively.

The systematic uncertainties in the BF measurement are discussed as follow.

- **Background shape:**
Since the $e^+e^- \rightarrow q\bar{q}$ and non- $D_s^{*\pm}D_s^\mp$ open charm processes are the major background sources, an alternative MC-simulated background shape is obtained by varying the relative fractions of the background components from these processes by the statistical uncertainties of their cross sections. The largest change, 0.5%, is taken as the related uncertainty.
- **Tracking and PID efficiency:**
The π^\pm and K^\pm tracking and PID efficiencies are studied with the control samples of $e^+e^- \rightarrow K^+K^-K^+K^-$, $K^+K^-\pi^+\pi^-(\pi^0)$, and $\pi^+\pi^-\pi^+\pi^-(\pi^0)$ decays. The data-MC tracking and PID efficiency ratios of $\pi^+(\pi^-)$ are 1.001 ± 0.003 (0.997 ± 0.003) and 0.998 ± 0.002 (0.998 ± 0.002), respectively. The data-MC tracking and PID efficiency ratios of $K^+(K^-)$ are 1.004 ± 0.006 (1.005 ± 0.006) and 0.998 ± 0.002 (0.998 ± 0.002), respectively. After correcting the MC efficiencies to data by these factors, the statistical uncertainties of the correction parameters are assigned to the systematic uncertainties associated with tracking and PID efficiencies. They are determined to be 0.3% (0.2%) for each π^+ (π^-), and 0.6% (0.2%) for each K^+ (K^-), respectively.
- **π^0 reconstruction:**
The π^0 reconstruction efficiency is investigated by using a control sample of the pro-

process $e^+e^- \rightarrow K^+K^-\pi^+\pi^-\pi^0$. The data-MC efficiency ratio for π^0 reconstruction is estimated to be 0.995 ± 0.008 . After correcting the efficiency by this factor, we assign 0.8% as the systematic uncertainty.

- MC sample size:

The uncertainty due to the limited MC sample size is obtained by $\sqrt{\sum_{\alpha} (f_{\alpha} \frac{\delta_{\epsilon_{\alpha}}}{\epsilon_{\alpha}})^2}$, where f_{α} is the tag yield fraction, and ϵ_{α} and $\delta_{\epsilon_{\alpha}}$ are the signal efficiency and the corresponding uncertainty of tag mode α , respectively. The uncertainty corresponding to MC statistics is 0.2%.

- Amplitude analysis model:

The uncertainty arising from the amplitude analysis model is estimated by varying the model parameters based on their error matrix. The distribution of 600 efficiencies resulting from this variation is fitted by a Gaussian function. The fitted width divided by the mean value, 0.4%, is taken as an uncertainty.

All of the systematic uncertainties are summarised in Table 11. Adding them in quadrature results in a total systematic uncertainty of 1.7%.

Source	Uncertainty (%)
Background shape	0.5
PID efficiency	0.6
Tracking efficiency	1.2
π^0 reconstruction	0.8
MC sample size	0.2
Amplitude model	0.4
Total	1.7

Table 11. Systematic uncertainties in the BF measurement.

6 Summary

The singly Cabibbo-suppressed decay $D_s^+ \rightarrow K^+\pi^+\pi^-\pi^0$ is observed, with a BF of $\mathcal{B}(D_s^+ \rightarrow K^+\pi^+\pi^-\pi^0) = (9.75 \pm 0.54_{\text{stat.}} \pm 0.17_{\text{syst.}}) \times 10^{-3}$. The first amplitude analysis is also performed, yielding FFs and phases for several significant intermediate states. Combining these results, we obtain the BFs presented in Table 12.

The dominant intermediate process is determined to be $D_s^+ \rightarrow K^{*0}\rho^+$, with a fraction of $(40.5 \pm 2.8_{\text{stat.}} \pm 1.5_{\text{syst.}})\%$. The decay $D_s^+ \rightarrow K^+\omega$ is observed with a significance greater than 10σ and its BF is measured to be $(0.95 \pm 0.12_{\text{stat.}} \pm 0.06_{\text{syst.}}) \times 10^{-3}$, which is consistent with the BESIII result $(0.87 \pm 0.24_{\text{stat.}} \pm 0.08_{\text{syst.}}) \times 10^{-3}$ [13] within 1σ , but the precision is improved by a factor of 2.1. Information about the two K_1 states in this decay provides inputs to further investigations of the mixing between these two axial-vector kaon states [15]. The asymmetry for the BFs of the decays $D_s^+ \rightarrow K^+\pi^+\pi^-\pi^0$ and $D_s^- \rightarrow K^-\pi^-\pi^+\pi^0$ is determined to be $(6.6 \pm 5.4_{\text{stat.}} \pm 0.7_{\text{syst.}})\%$. No evidence for CP violation is found under the current sample size.

Intermediate process	BF (10^{-3})
$D_s^+[S] \rightarrow K^*(892)^0 \rho^+$	$1.41 \pm 0.23 \pm 0.07$
$D_s^+[P] \rightarrow K^*(892)^0 \rho^+$	$2.53 \pm 0.28 \pm 0.12$
$D_s^+ \rightarrow K^*(892)^0 \rho^+$	$3.95 \pm 0.35 \pm 0.17$
$D_s^+[P] \rightarrow K^*(892)^+ \rho^0$	$0.42 \pm 0.16 \pm 0.06$
$D_s^+ \rightarrow K^+ \omega$	$0.95 \pm 0.12 \pm 0.06$
$D_s^+ \rightarrow K_1(1270)^0 \pi^+, K_1(1270)^0[S] \rightarrow K^+ \rho^-$	$0.39 \pm 0.12 \pm 0.06$
$D_s^+ \rightarrow K_1(1400)^0 \pi^+, K_1(1400)^0[S] \rightarrow K^*(892)^+ \pi^-$	$0.55 \pm 0.09 \pm 0.03$
$D_s^+ \rightarrow K_1(1400)^0 \pi^+, K_1(1400)^0[S] \rightarrow K^*(892)^0 \pi^0$	$0.59 \pm 0.09 \pm 0.02$
$D_s^+ \rightarrow K_1(1400)^0 \pi^+, K_1(1400)^0[S] \rightarrow K^*(892) \pi$	$1.10 \pm 0.19 \pm 0.04$
$D_s^+ \rightarrow a_1(1260)^0 K^+, a_1(1260)^0[S] \rightarrow \rho^+ \pi^-$	$0.19 \pm 0.07 \pm 0.09$
$D_s^+ \rightarrow a_1(1260)^0 K^+, a_1(1260)^0[S] \rightarrow \rho^- \pi^+$	$0.19 \pm 0.07 \pm 0.09$
$D_s^+ \rightarrow a_1(1260)^0 K^+, a_1(1260)^0[S] \rightarrow \rho \pi$	$0.32 \pm 0.12 \pm 0.15$
$D_s^+[S] \rightarrow (K^+ \pi^0)_V \rho^0$	$1.01 \pm 0.20 \pm 0.06$
$D_s^+ \rightarrow (K^+ \pi^0)_{S\text{-wave}} (\pi^+ \pi^-)_{S\text{-wave}}$	$0.93 \pm 0.22 \pm 0.09$

Table 12. The BFs for various intermediate processes in the hadronic decay of $D_s^+ \rightarrow K^+ \pi^+ \pi^- \pi^0$. The first and second uncertainties are statistical and systematic, respectively.

Acknowledgments

The BESIII collaboration thanks the staff of BEPCII and the IHEP computing center for their strong support. This work is supported in part by National Key Research and Development Program of China under Contracts Nos. 2020YFA0406400, 2020YFA0406300; National Natural Science Foundation of China (NSFC) under Contracts Nos. 11625523, 11635010, 11735014, 11775027, 11822506, 11835012, 11875054, 11935015, 11935016, 11935018, 11961141012, 12192260, 12192261, 12192262, 12192263, 12192264, 12192265; the Chinese Academy of Sciences (CAS) Large-Scale Scientific Facility Program; Joint Large-Scale Scientific Facility Funds of the NSFC and CAS under Contracts Nos. U1732263, U1832207, U2032104; CAS Key Research Program of Frontier Sciences under Contracts Nos. QYZDJ-SSW-SLH003, QYZDJ-SSW-SLH040; 100 Talents Program of CAS; INPAC and Shanghai Key Laboratory for Particle Physics and Cosmology; ERC under Contract No. 758462; European Union Horizon 2020 research and innovation programme under Contract No. Marie Skłodowska-Curie grant agreement No 894790; German Research Foundation DFG under Contracts Nos. 443159800, Collaborative Research Center CRC 1044, FOR 2359, FOR 2359, GRK 214; Istituto Nazionale di Fisica Nucleare, Italy; Ministry of Development of Turkey under Contract No. DPT2006K-120470; National Science and Technology fund; Olle Engkvist Foundation under Contract No. 200-0605; STFC (United Kingdom); The Knut and Alice Wallenberg Foundation (Sweden) under Contract No. 2016.0157; The Royal Society, UK under Contracts Nos. DH140054, DH160214; The Swedish Research Council; U. S. Department of Energy under Contracts Nos. DE-FG02-05ER41374, DE-SC-0012069.

References

- [1] G. Goldhaber et al., *Observation in e^+e^- Annihilation of a Narrow State at $1865\text{-MeV}/c^{**2}$ Decaying to $K\pi$ and $K\pi\pi\pi$* , *Phys. Rev. Lett.* **37** (1976) 255.
- [2] I. Peruzzi et al., *Observation of a Narrow Charged State at $1876\text{-MeV}/c^{**2}$ Decaying to an Exotic Combination of $K\pi\pi$* , *Phys. Rev. Lett.* **37** (1976) 569.
- [3] H.-Y. Cheng and C.-W. Chiang, *Two-body hadronic charmed meson decays*, *Phys. Rev. D* **81** (2010) 074021.
- [4] PARTICLE DATA GROUP collaboration, *Review of Particle Physics*, *PTEP* **2020** (2020) 083C01.
- [5] M. Bauer, B. Stech and M. Wirbel, *Exclusive Nonleptonic Decays of D , $D(s)$, and B Mesons*, *Z. Phys. C* **34** (1987) 103.
- [6] A. N. Kamal, R. C. Verma and N. Sinha, *$(D, D(s)^+) \rightarrow VV$ decays in two models: An $SU(3)$ symmetry model and a factorization model with final state interactions*, *Phys. Rev. D* **43** (1991) 843.
- [7] I. Hinchliffe and T. A. Kaeding, *Nonleptonic two-body decays of D mesons in broken $SU(3)$* , *Phys. Rev. D* **54** (1996) 914 [[hep-ph/9502275](#)].
- [8] E. H. E. Aaoud and A. N. Kamal, *Helicity and partial wave amplitude analysis of $D \rightarrow K^*\rho$ decay*, *Phys. Rev. D* **59** (1999) 114013 [[hep-ph/9910350](#)].
- [9] X.-W. Kang and H.-B. Li, *Study of CP violation in $D \rightarrow VV$ decay at BESIII*, *Phys. Lett. B* **684** (2010) 137 [[arXiv:0912.3068](#)].
- [10] H.-Y. Cheng, *Revisiting Axial-Vector Meson Mixing*, *Phys. Lett. B* **707** (2012) 116 [[arXiv:1110.2249](#)].
- [11] H.-Y. Cheng and C.-W. Chiang, *Revisiting CP violation in $D \rightarrow PP$ and VP decays*, *Phys. Rev. D* **100** (2019) 093002 [[arXiv:1909.03063](#)].
- [12] Q. Qin, H.-n. Li, C.-D. Lü and F.-S. Yu, *Branching ratios and direct CP asymmetries in $D \rightarrow PV$ decays*, *Phys. Rev. D* **89** (2014) 054006 [[arXiv:1305.7021](#)].
- [13] BESIII collaboration, *Observation of the W -Annihilation Decay $D_s^+ \rightarrow \omega\pi^+$ and Evidence for $D_s^+ \rightarrow \omega K^+$* , *Phys. Rev. D* **99** (2019) 091101 [[arXiv:1811.00392](#)].
- [14] H.-Y. Cheng and C.-W. Chiang, *CP violation in quasi-two-body $D \rightarrow VP$ decays and three-body D decays mediated by vector resonances*, *Phys. Rev. D* **104** (2021) 073003 [[arXiv:2104.13548](#)].
- [15] H.-Y. Cheng, C.-W. Chiang and A.-L. Kuo, *Global analysis of two-body $D \rightarrow VP$ decays within the framework of flavor symmetry*, *Phys. Rev. D* **93** (2016) 114010 [[arXiv:1604.03761](#)].
- [16] M. Ablikim, Z. An, J. Bai, N. Berger, J. Bian, X. Cai et al., *Design and construction of the BESIII detector*, *Nucl. Instrum. Meth. A* **614** (2010) 345.
- [17] BESIII collaboration, *Future physics programme of BESIII*, *Chin. Phys. C* **44** (2020) 040001 [[arXiv:1912.05983](#)].
- [18] C. Yu et al., *BEPCII Performance and Beam Dynamics Studies on Luminosity*, in *Proc. of International Particle Accelerator Conference (IPAC'16), Busan, Korea, May 8-13, 2016*, no. 7 in International Particle Accelerator Conference, (Geneva, Switzerland), pp. 1014–1018, JACoW, June, 2016, [DOI](#).

- [19] X. Li, Y. Sun, C. Li, Z. Liu, Y. Heng, M. Shao et al., *Study of MRPC technology for BESIII endcap-TOF upgrade*, *Radiat. Detect. Technol. Methods* **1** (2017) 13.
- [20] Y.-X. Guo, S.-S. Sun, F.-F. An, R.-X. Yang, M. Zhou, Z. Wu et al., *The study of time calibration for upgraded end cap TOF of BESIII*, *Radiat. Detect. Technol. Methods* **1** (2017) 15.
- [21] P. Cao, H. Chen, M. Chen, H. Dai, Y. Heng, X. Ji et al., *Design and construction of the new besiii endcap time-of-flight system with mrpc technology*, *Nucl. Instrum. Meth. A* **953** (2020) 163053.
- [22] BESIII collaboration, *Measurements of integrated luminosities at BESIII for data samples at collision energies around 4 GeV*, [arXiv:2203.03133](https://arxiv.org/abs/2203.03133).
- [23] BESIII collaboration, *Precision measurement of the integrated luminosity of the data taken by BESIII at center of mass energies between 3.810 GeV and 4.600 GeV*, *Chin. Phys. C* **39** (2015) 093001 [[arXiv:1503.03408](https://arxiv.org/abs/1503.03408)].
- [24] BESIII collaboration, *Measurement of the center-of-mass energies at BESIII via the di-muon process*, *Chin. Phys. C* **40** (2016) 063001 [[arXiv:1510.08654](https://arxiv.org/abs/1510.08654)].
- [25] CLEO collaboration, *Measurement of charm production cross sections in e^+e^- annihilation at energies between 3.97 and 4.26 GeV*, *Phys. Rev. D* **80** (2009) 072001.
- [26] GEANT4 collaboration, *GEANT4 – a simulation toolkit*, *Nucl. Instrum. Meth. A* **506** (2003) 250.
- [27] S. Jadach, B. F. L. Ward and Z. Wař, *Coherent exclusive exponentiation for precision monte carlo calculations*, *Phys. Rev. D* **63** (2001) 113009.
- [28] S. Jadach, B. F. L. Ward and Z. Wař, *The precision monte carlo event generator *kk* for two-fermion final states in e^+e^- collisions*, *Computer Physics Communications* **130** (2000) 260.
- [29] D. Lange, *The EvtGen particle decay simulation package*, *Nucl. Instrum. Meth. A* **462** (2001) 152.
- [30] R.-G. Ping, *Event generators at BESIII*, *Chin. Phys. C* **32** (2008) 599.
- [31] J. C. Chen, G. S. Huang, X. R. Qi, D. H. Zhang and Y. S. Zhu, *Event generator for J/ψ and $\psi(2S)$ decay*, *Phys. Rev. D* **62** (2000) 034003.
- [32] R.-L. Yang, R.-G. Ping and H. Chen, *Tuning and validation of the Lundcharm model with J/ψ decays*, *Chin. Phys. Lett.* **31** (2014) 061301.
- [33] E. Richter-Was, *QED bremsstrahlung in semileptonic B and leptonic τ decays*, *Phys. Lett. B* **303** (1993) 163 .
- [34] MARK-III collaboration, *Direct Measurements of Charmed d Meson Hadronic Branching Fractions*, *Phys. Rev. Lett.* **56** (1986) 2140.
- [35] B. S. Zou and D. V. Bugg, *Covariant tensor formalism for partial wave analyses of psi decay to mesons*, *Eur. Phys. J. A* **16** (2003) 537 [[hep-ph/0211457](https://arxiv.org/abs/hep-ph/0211457)].
- [36] K. Cranmer, *Kernel estimation in high-energy physics*, *Computer Physics Communications* **136** (2001) 198.
- [37] W. Verkerke and D. P. Kirkby, *RooFit Users Manual v2.91*.
http://roofit.sourceforge.net/docs/RooFit_Users_Manual_2.91-33.pdf.

- [38] BESIII collaboration, *Amplitude analysis and branching fraction measurement of $D_s^+ \rightarrow K^+ K^- \pi^+$* , *Phys. Rev. D* **104** (2021) 012016 [[arXiv:2011.08041](#)].
- [39] LHCb collaboration, *Studies of the resonance structure in $D^0 \rightarrow K^\mp \pi^\pm \pi^\pm \pi^\mp$ decays*, *Eur. Phys. J. C* **78** (2018) 443 [[arXiv:1712.08609](#)].
- [40] G. J. Gounaris and J. J. Sakurai, *Finite-width corrections to the vector-meson-dominance prediction for $\rho \rightarrow e^+ e^-$* , *Phys. Rev. Lett.* **21** (1968) 244.
- [41] I. J. R. Aitchison, *K-MATRIX FORMALISM FOR OVERLAPPING RESONANCES*, *Nucl. Phys. A* **189** (1972) 417.
- [42] J. Back et al., *LAURA⁺⁺: A Dalitz plot fitter*, *Comput. Phys. Commun.* **231** (2018) 198 [[arXiv:1711.09854](#)].
- [43] V. V. Anisovich and A. V. Sarantsev, *K matrix analysis of the $(I J^{**}(PC) = 00^{++})$ -wave in the mass region below 1900 MeV*, *Eur. Phys. J. A* **16** (2003) 229 [[hep-ph/0204328](#)].
- [44] LHCb collaboration, *Amplitude analysis of the $B^+ \rightarrow \pi^+ \pi^+ \pi^-$ decay*, *Phys. Rev. D* **101** (2020) 012006 [[arXiv:1909.05212](#)].
- [45] BABAR, BELLE collaboration, *Measurement of $\cos 2\beta$ in $B^0 \rightarrow D^{(*)} h^0$ with $D \rightarrow K_S^0 \pi^+ \pi^-$ decays by a combined time-dependent Dalitz plot analysis of BaBar and Belle data*, *Phys. Rev. D* **98** (2018) 112012 [[arXiv:1804.06153](#)].
- [46] A. V. Anisovich and A. V. Sarantsev, *K matrix analysis of the $K \pi S$ wave in the mass region 900-MeV - 2100-MeV and nonet classification of scalar q anti- q states*, *Phys. Lett. B* **413** (1997) 137 [[hep-ph/9705401](#)].

Index	Amplitude	Relation
A_1	$D_s^+ \rightarrow K_1(1400)^0 \pi^+, K_1(1400)^0 \rightarrow K^*(892)^0 \pi^0$	
A_2	$D_s^+ \rightarrow K_1(1400)^0 \pi^+, K_1(1400)^0 \rightarrow K^*(892)^+ \pi^-$	
A	$D_s^+ \rightarrow K_1(1400)^0 \pi^+, K_1(1400)^0 \rightarrow K^* \pi$	$A_1 - A_2$
A_1	$D_s^+ \rightarrow a_1(1260)^0 \pi^+, a_1(1260)^0 \rightarrow \rho^+ \pi^-$	
A_2	$D_s^+ \rightarrow a_1(1260)^0 \pi^+, a_1(1260)^0 \rightarrow \rho^- \pi^+$	
A	$D_s^+ \rightarrow a_1(1260)^0 \pi^+, a_1(1260)^0 \rightarrow \rho \pi$	$A_1 - A_2$

Table 13. The Clebsch-Gordan (CG) relations used.

A Clebsch-Gordan relation

Considering the isospin relationship in hadron decays, some amplitudes are fixed by Clebsch-Gordan relations, as listed in Table 13. The amplitudes with fixed relations share the same magnitude (ρ) and phase (ϕ).

B Other intermediate processes tested

Some other tested amplitudes with significance less than 3σ are listed below, the value in each of brackets corresponds to the significance.

• Cascade amplitudes

- $D_s^+ \rightarrow K^*(892)^+ f_0(500), K^*(892)^+ \rightarrow K^+ \pi^0, f_0(500) \rightarrow \pi^+ \pi^-$ ($< 1\sigma$)
- $D_s^+ \rightarrow K^*(892)^+ f_0(980), K^*(892)^+ \rightarrow K^+ \pi^0, f_0(980) \rightarrow \pi^+ \pi^-$ ($< 1\sigma$)
- $D_s^+[D] \rightarrow K^*(892)^0 \rho^+, K^*(892)^0 \rightarrow K^+ \pi^-, \rho^+ \rightarrow \pi^+ \pi^0$ (2.6σ)
- $D_s^+[S, D] \rightarrow K^*(892)^+ \rho^0, K^*(892)^+ \rightarrow K^+ \pi^0, \rho^0 \rightarrow \pi^+ \pi^-$ (2.0σ)
- $D_s^+ \rightarrow \pi^+ K_1(1270)^0, K_1(1270)^0[D] \rightarrow K^+ \rho^-$ (1.5σ)
- $D_s^+ \rightarrow \pi^0 K_1(1270)^+, K_1(1270)^+[S, D] \rightarrow K^+ \rho^0$ ($< 1\sigma$)
- $D_s^+ \rightarrow \pi^+ K_1(1400)^0, K_1(1400)^0[D] \rightarrow K^* \pi$ (2.0σ)
- $D_s^+ \rightarrow \pi^+ K_1(1650)^0, K_1(1650)^0[S, D] \rightarrow K^* \pi$ (2.7σ)
- $D_s^+ \rightarrow K^*(1410)^0 \pi^+, K^*(1410)^0 \rightarrow K^* \pi$ (1.9σ)
- $D_s^+ \rightarrow K^*(1410)^0 \pi^+, K^*(1410)^0 \rightarrow K^+ \rho^-$ ($< 1\sigma$)
- $D_s^+ \rightarrow K^*(1410)^+ \pi^0, K^*(1410)^+ \rightarrow K^* \pi$ (1.9σ)
- $D_s^+ \rightarrow K^*(1410)^+ \pi^0, K^*(1410)^+ \rightarrow K^+ \rho^0$ (1.8σ)
- $D_s^+ \rightarrow K^0(1460) \pi^+, K^0(1460) \rightarrow K^* \pi$ ($< 1\sigma$)
- $D_s^+ \rightarrow K^0(1460) \pi^+, K^0(1460) \rightarrow K^+ \rho^-$ ($< 1\sigma$)
- $D_s^+ \rightarrow K^*(1680)^0 \pi^+, K^*(1680)^0 \rightarrow K^* \pi$ (2.3σ)
- $D_s^+ \rightarrow K^*(1680)^+ \pi^0, K^*(1680)^0 \rightarrow K^+ \rho^-$ (2.0σ)

- $D_s^+ \rightarrow K^+ h_1(1170), h_1(1170)[S, D] \rightarrow \rho\pi (< 1\sigma)$
- $D_s^+ \rightarrow K^+ a_1(1260), a_1(1260)[D] \rightarrow \rho\pi (< 1\sigma)$
- $D_s^+ \rightarrow K^+ \pi^0(1300), \pi^0(1300) \rightarrow \rho\pi (2.3\sigma)$
- $D_s^+ \rightarrow K^+ a_2(1320), a_2(1320) \rightarrow \rho\pi (1.4\sigma)$
- $D_s^+ \rightarrow K^+ a_2(1320), a_2(1320) \rightarrow \rho(1450)\pi (1.5\sigma)$
- $D_s^+ \rightarrow K^+ \omega(1420), \omega(1420) \rightarrow \rho\pi (< 1\sigma)$

• **Three-body amplitudes**

- $D_s^+[S] \rightarrow K^*(892)^+(\pi^+\pi^-)_V (2.2\sigma)$
- $D_s^+[P] \rightarrow K^*(892)^+(\pi^+\pi^-)_V (2.2\sigma)$
- $D_s^+[D] \rightarrow K^*(892)^+(\pi^+\pi^-)_V (2.0\sigma)$
- $D_s^+[S] \rightarrow K^*(892)^0(\pi^+\pi^0)_V (2.0\sigma)$
- $D_s^+[P] \rightarrow K^*(892)^0(\pi^+\pi^0)_V (< 1\sigma)$
- $D_s^+[D] \rightarrow K^*(892)^0(\pi^+\pi^0)_V (3.0\sigma)$
- $D_s^+[S] \rightarrow \rho^+(K^+\pi^-)_V (< 1\sigma)$
- $D_s^+[P] \rightarrow \rho^+(K^+\pi^-)_V (1.8\sigma)$
- $D_s^+[D] \rightarrow \rho^+(K^+\pi^-)_V (< 1\sigma)$
- $D_s^+[P] \rightarrow \rho^0(K^+\pi^0)_V (2.0\sigma)$
- $D_s^+[D] \rightarrow \rho^0(K^+\pi^0)_V (1.8\sigma)$
- $D_s^+ \rightarrow K^*(892)^+(\pi^+\pi^-)_{S\text{-wave}} (2.0\sigma)$
- $D_s^+ \rightarrow K^*(892)^0(\pi^+\pi^0)_{S\text{-wave}} (1.9\sigma)$
- $D_s^+ \rightarrow \rho^+(K^+\pi^-)_{S\text{-wave}} (2.3\sigma)$
- $D_s^+ \rightarrow \rho^0(K^+\pi^0)_{S\text{-wave}} (< 1\sigma)$

• **Four-body non-resonance amplitudes**

- $D_s^+ \rightarrow K^+((\pi^+\pi^-)_{S\text{-wave}}\pi^0)_A (< 1\sigma)$
- $D_s^+ \rightarrow K^+((\pi^+\pi^-)_{S\text{-wave}}\pi^0)_P (1.6\sigma)$
- $D_s^+ \rightarrow \pi^0((\pi^+\pi^-)_{S\text{-wave}}K^+)_A (1.8\sigma)$
- $D_s^+ \rightarrow \pi^0((\pi^+\pi^-)_{S\text{-wave}}K^+)_P (1.9\sigma)$
- $D_s^+ \rightarrow \pi^0((K^+\pi^-)_{S\text{-wave}}\pi^+)_A (< 1\sigma)$
- $D_s^+ \rightarrow \pi^0((K^+\pi^-)_{S\text{-wave}}\pi^+)_P (< 1\sigma)$
- $D_s^+ \rightarrow \pi^+((K^+\pi^-)_{S\text{-wave}}\pi^0)_A (2.3\sigma)$
- $D_s^+ \rightarrow \pi^+((K^+\pi^-)_{S\text{-wave}}\pi^0)_P (2.0\sigma)$
- $D_s^+ \rightarrow \pi^+((K^+\pi^0)_{S\text{-wave}}\pi^-)_A (< 1\sigma)$
- $D_s^+ \rightarrow \pi^+((K^+\pi^0)_{S\text{-wave}}\pi^-)_P (< 1\sigma)$

BESIII Collaboration

M. Ablikim¹, M. N. Achasov^{11,b}, P. Adlarson⁷⁰, M. Albrecht⁴, R. Aliberti³¹, A. Amoroso^{69A,69C}, M. R. An³⁵, Q. An^{66,53}, X. H. Bai⁶¹, Y. Bai⁵², O. Bakina³², R. Baldini Ferroli^{26A}, I. Balossino^{27A}, Y. Ban^{42,g}, V. Batozskaya^{1,40}, D. Becker³¹, K. Begzsuren²⁹, N. Berger³¹, M. Bertani^{26A}, D. Bettoni^{27A}, F. Bianchi^{69A,69C}, J. Bloms⁶³, A. Bortone^{69A,69C}, I. Boyko³², R. A. Briere⁵, A. Brueggemann⁶³, H. Cai⁷¹, X. Cai^{1,53}, A. Calcaterra^{26A}, G. F. Cao^{1,58}, N. Cao^{1,58}, S. A. Cetin^{57A}, J. F. Chang^{1,53}, W. L. Chang^{1,58}, G. Chelkov^{32,a}, C. Chen³⁹, Chao Chen⁵⁰, G. Chen¹, H. S. Chen^{1,58}, M. L. Chen^{1,53,58}, S. J. Chen³⁸, S. M. Chen⁵⁶, T. Chen^{1,58}, X. R. Chen^{28,58}, X. T. Chen^{1,58}, Y. B. Chen^{1,53}, Z. J. Chen^{23,h}, W. S. Cheng^{69C}, X. Chu³⁹, G. Cibinetto^{27A}, F. Cossio^{69C}, J. J. Cui⁴⁵, H. L. Dai^{1,53}, J. P. Dai⁷³, A. Dbeyssi¹⁷, R. E. de Boer⁴, D. Dedovich³², Z. Y. Deng¹, A. Denig³¹, I. Denysenko³², M. Destefanis^{69A,69C}, F. De Mori^{69A,69C}, Y. Ding³⁶, J. Dong^{1,53}, L. Y. Dong^{1,58}, M. Y. Dong^{1,53,58}, X. Dong⁷¹, S. X. Du⁷⁵, P. Egorov^{32,a}, Y. L. Fan⁷¹, J. Fang^{1,53}, S. S. Fang^{1,58}, W. X. Fang¹, Y. Fang¹, R. Farinelli^{27A}, L. Fava^{69B,69C}, F. Feldbauer⁴, G. Felici^{26A}, C. Q. Feng^{66,53}, J. H. Feng⁵⁴, K. Fischer⁶⁴, M. Fritsch⁴, C. Fritsch⁶³, C. D. Fu¹, H. Gao⁵⁸, Y. N. Gao^{42,g}, Yang Gao^{66,53}, S. Garbolino^{69C}, I. Garzia^{27A,27B}, P. T. Ge⁷¹, Z. W. Ge³⁸, C. Geng⁵⁴, E. M. Gersabeck⁶², A. Gilman⁶⁴, K. Goetzen¹², L. Gong³⁶, W. X. Gong^{1,53}, W. Gradl³¹, M. Greco^{69A,69C}, L. M. Gu³⁸, M. H. Gu^{1,53}, Y. T. Gu¹⁴, C. Y. Guan^{1,58}, A. Q. Guo^{28,58}, L. B. Guo³⁷, R. P. Guo⁴⁴, Y. P. Guo^{10,f}, A. Guskov^{32,a}, T. T. Han⁴⁵, W. Y. Han³⁵, X. Q. Hao¹⁸, F. A. Harris⁶⁰, K. K. He⁵⁰, K. L. He^{1,58}, F. H. Heinsius⁴, C. H. Heinz³¹, Y. K. Heng^{1,53,58}, C. Herold⁵⁵, M. Himmelreich^{12,d}, G. Y. Hou^{1,58}, Y. R. Hou⁵⁸, Z. L. Hou¹, H. M. Hu^{1,58}, J. F. Hu^{51,i}, T. Hu^{1,53,58}, Y. Hu¹, G. S. Huang^{66,53}, K. X. Huang⁵⁴, L. Q. Huang^{28,58}, L. Q. Huang⁶⁷, X. T. Huang⁴⁵, Y. P. Huang¹, T. Hussain⁶⁸, N. Hüskens^{25,31}, W. Imoehl²⁵, M. Irshad^{66,53}, J. Jackson²⁵, S. Jaeger⁴, S. Janchiv²⁹, Q. Ji¹, Q. P. Ji¹⁸, X. B. Ji^{1,58}, X. L. Ji^{1,53}, Y. Y. Ji⁴⁵, Z. K. Jia^{66,53}, H. B. Jiang⁴⁵, S. S. Jiang³⁵, X. S. Jiang^{1,53,58}, Y. Jiang⁵⁸, J. B. Jiao⁴⁵, Z. Jiao²¹, S. Jin³⁸, Y. Jin⁶¹, M. Q. Jing^{1,58}, T. Johansson⁷⁰, N. Kalantar-Nayestanaki⁵⁹, X. S. Kang³⁶, R. Kappert⁵⁹, M. Kavatsyuk⁵⁹, B. C. Ke⁷⁵, I. K. Keshk⁴, A. Khoukaz⁶³, P. Kiese³¹, R. Kiuchi¹, R. Kliemt¹², L. Koch³³, O. B. Kolcu^{57A}, B. Kopf⁴, M. Kuemmel⁴, M. Kuessner⁴, A. Kupsc^{40,70}, W. Kühn³³, J. J. Lane⁶², J. S. Lange³³, P. Larin¹⁷, A. Lavania²⁴, L. Lavezzi^{69A,69C}, Z. H. Lei^{66,53}, H. Leithoff³¹, M. Lellmann³¹, T. Lenz³¹, C. Li⁴³, C. Li³⁹, C. H. Li³⁵, Cheng Li^{66,53}, D. M. Li⁷⁵, F. Li^{1,53}, G. Li¹, H. Li^{66,53}, H. B. Li^{1,58}, H. J. Li¹⁸, H. N. Li^{51,i}, J. Q. Li⁴, J. S. Li⁵⁴, J. W. Li⁴⁵, Ke Li¹, L. J Li^{1,58}, L. K. Li¹, Lei Li³, M. H. Li³⁹, P. R. Li^{34,j,k}, S. X. Li¹⁰, S. Y. Li⁵⁶, T. Li⁴⁵, W. D. Li^{1,58}, W. G. Li¹, X. H. Li^{66,53}, X. L. Li⁴⁵, Xiaoyu Li^{1,58}, Z. Y. Li⁵⁴, H. Liang³⁰, H. Liang^{1,58}, H. Liang^{66,53}, Y. F. Liang⁴⁹, Y. T. Liang^{28,58}, G. R. Liao¹³, L. Z. Liao⁴⁵, J. Libby²⁴, A. Limphirat⁵⁵, D. X. Lin^{28,58}, T. Lin¹, B. J. Liu¹, C. X. Liu¹, D. Liu^{17,66}, F. H. Liu⁴⁸, Fang Liu¹, Feng Liu⁶, G. M. Liu^{51,i}, H. Liu^{34,j,k}, H. B. Liu¹⁴, H. M. Liu^{1,58}, Huanhuan Liu¹, Huihui Liu¹⁹, J. B. Liu^{66,53}, J. L. Liu⁶⁷, J. Y. Liu^{1,58}, K. Liu¹, K. Y. Liu³⁶, Ke Liu²⁰, L. Liu^{66,53}, Lu Liu³⁹, M. H. Liu^{10,f}, P. L. Liu¹, Q. Liu⁵⁸, S. B. Liu^{66,53}, T. Liu^{10,f}, W. K. Liu³⁹, W. M. Liu^{66,53}, X. Liu^{34,j,k}, Y. Liu^{34,j,k}, Y. B. Liu³⁹, Z. A. Liu^{1,53,58}, Z. Q. Liu⁴⁵, X. C. Lou^{1,53,58}, F. X. Lu⁵⁴, H. J. Lu²¹, J. G. Lu^{1,53}, X. L. Lu¹, Y. Lu⁷, Y. P. Lu^{1,53}, Z. H. Lu^{1,58}, C. L. Luo³⁷, M. X. Luo⁷⁴, T. Luo^{10,f}, X. L. Luo^{1,53}, X. R. Lyu⁵⁸, Y. F. Lyu³⁹, F. C. Ma³⁶, H. L. Ma¹, L. L. Ma⁴⁵, M. M. Ma^{1,58}, Q. M. Ma¹, R. Q. Ma^{1,58},

R. T. Ma⁵⁸, X. Y. Ma^{1,53}, Y. Ma^{42,g}, F. E. Maas¹⁷, M. Maggiora^{69A,69C}, S. Maldaner⁴,
 S. Malde⁶⁴, Q. A. Malik⁶⁸, A. Mangoni^{26B}, Y. J. Mao^{42,g}, Z. P. Mao¹, S. Marcello^{69A,69C},
 Z. X. Meng⁶¹, J. G. Messchendorp^{59,12}, G. Mezzadri^{27A}, H. Miao^{1,58}, T. J. Min³⁸, R. E. Mitchell²⁵,
 X. H. Mo^{1,53,58}, N. Yu. Muchnoi^{11,b}, Y. Nefedov³², F. Nerling^{17,d}, I. B. Nikolaev^{11,b}, Z. Ning^{1,53},
 S. Nisar^{9,l}, Y. Niu⁴⁵, S. L. Olsen⁵⁸, Q. Ouyang^{1,53,58}, S. Pacetti^{26B,26C}, X. Pan^{10,f},
 Y. Pan⁶², A. Pathak³⁰, M. Pelizaeus⁴, H. P. Peng^{66,53}, K. Peters^{12,d}, J. L. Ping³⁷, R. G. Ping^{1,58},
 S. Plura³¹, S. Pogodin³², V. Prasad^{66,53}, F. Z. Qi¹, H. Qi^{66,53}, H. R. Qi⁵⁶, M. Qi³⁸,
 T. Y. Qi^{10,f}, S. Qian^{1,53}, W. B. Qian⁵⁸, Z. Qian⁵⁴, C. F. Qiao⁵⁸, J. J. Qin⁶⁷, L. Q. Qin¹³,
 X. P. Qin^{10,f}, X. S. Qin⁴⁵, Z. H. Qin^{1,53}, J. F. Qiu¹, S. Q. Qu⁵⁶, K. H. Rashid⁶⁸, C. F. Redmer³¹,
 K. J. Ren³⁵, A. Rivetti^{69C}, V. Rodin⁵⁹, M. Rolo^{69C}, G. Rong^{1,58}, Ch. Rosner¹⁷, S. N. Ruan³⁹,
 A. Sarantsev^{32,c}, Y. Schelhaas³¹, C. Schnier⁴, K. Schoenning⁷⁰, M. Scodreggio^{27A,27B}, K. Y. Shan^{10,f},
 W. Shan²², X. Y. Shan^{66,53}, J. F. Shangguan⁵⁰, L. G. Shao^{1,58}, M. Shao^{66,53}, C. P. Shen^{10,f},
 H. F. Shen^{1,58}, X. Y. Shen^{1,58}, B. A. Shi⁵⁸, H. C. Shi^{66,53}, J. Y. Shi¹, Q. Q. Shi⁵⁰,
 R. S. Shi^{1,58}, X. Shi^{1,53}, X. D. Shi^{66,53}, J. J. Song¹⁸, W. M. Song^{30,1}, Y. X. Song^{42,g},
 S. Sosio^{69A,69C}, S. Spataro^{69A,69C}, F. Stieler³¹, K. X. Su⁷¹, P. P. Su⁵⁰, Y. J. Su⁵⁸, G. X. Sun¹,
 H. Sun⁵⁸, H. K. Sun¹, J. F. Sun¹⁸, L. Sun⁷¹, S. S. Sun^{1,58}, T. Sun^{1,58}, W. Y. Sun³⁰,
 X. Sun^{23,h}, Y. J. Sun^{66,53}, Y. Z. Sun¹, Z. T. Sun⁴⁵, Y. H. Tan⁷¹, Y. X. Tan^{66,53}, C. J. Tang⁴⁹,
 G. Y. Tang¹, J. Tang⁵⁴, L. Y. Tao⁶⁷, Q. T. Tao^{23,h}, J. X. Teng^{66,53}, V. Thoren⁷⁰, W. H. Tian⁴⁷,
 Y. Tian^{28,58}, I. Uman^{57B}, B. Wang¹, B. L. Wang⁵⁸, C. W. Wang³⁸, D. Y. Wang^{42,g},
 F. Wang⁶⁷, H. J. Wang^{34,j,k}, H. P. Wang^{1,58}, K. Wang^{1,53}, L. L. Wang¹, M. Wang⁴⁵,
 Meng Wang^{1,58}, S. Wang¹³, S. Wang^{10,f}, T. Wang^{10,f}, T. J. Wang³⁹, W. Wang⁵⁴, W. H. Wang⁷¹,
 W. P. Wang^{66,53}, X. Wang^{42,g}, X. F. Wang^{34,j,k}, X. L. Wang^{10,f}, Y. Wang⁵⁶, Y. D. Wang⁴¹,
 Y. F. Wang^{1,53,58}, Y. H. Wang⁴³, Y. Q. Wang¹, Yaqian Wang^{16,1}, Z. Wang^{1,53}, Z. Y. Wang^{1,58},
 Ziyi Wang⁵⁸, D. H. Wei¹³, F. Weidner⁶³, S. P. Wen¹, D. J. White⁶², U. Wiedner⁴, G. Wilkinson⁶⁴,
 M. Wolke⁷⁰, L. Wollenberg⁴, J. F. Wu^{1,58}, L. H. Wu¹, L. J. Wu^{1,58}, X. Wu^{10,f}, X. H. Wu³⁰,
 Y. Wu⁶⁶, Y. J. Wu²⁸, Z. Wu^{1,53}, L. Xia^{66,53}, T. Xiang^{42,g}, D. Xiao^{34,j,k}, G. Y. Xiao³⁸,
 H. Xiao^{10,f}, S. Y. Xiao¹, Y. L. Xiao^{10,f}, Z. J. Xiao³⁷, C. Xie³⁸, X. H. Xie^{42,g}, Y. Xie⁴⁵,
 Y. G. Xie^{1,53}, Y. H. Xie⁶, Z. P. Xie^{66,53}, T. Y. Xing^{1,58}, C. F. Xu^{1,58}, C. J. Xu⁵⁴, G. F. Xu¹,
 H. Y. Xu⁶¹, Q. J. Xu¹⁵, X. P. Xu⁵⁰, Y. C. Xu⁵⁸, Z. P. Xu³⁸, F. Yan^{10,f}, L. Yan^{10,f},
 W. B. Yan^{66,53}, W. C. Yan⁷⁵, H. J. Yang^{46,e}, H. L. Yang³⁰, H. X. Yang¹, L. Yang⁴⁷,
 S. L. Yang⁵⁸, Tao Yang¹, Y. F. Yang³⁹, Y. X. Yang^{1,58}, Yifan Yang^{1,58}, M. Ye^{1,53}, M. H. Ye⁸,
 J. H. Yin¹, Z. Y. You⁵⁴, B. X. Yu^{1,53,58}, C. X. Yu³⁹, G. Yu^{1,58}, T. Yu⁶⁷, C. Z. Yuan^{1,58},
 L. Yuan², S. C. Yuan¹, X. Q. Yuan¹, Y. Yuan^{1,58}, Z. Y. Yuan⁵⁴, C. X. Yue³⁵, A. A. Zafar⁶⁸,
 F. R. Zeng⁴⁵, X. Zeng⁶, Y. Zeng^{23,h}, Y. H. Zhan⁵⁴, A. Q. Zhang^{1,58}, B. L. Zhang^{1,58},
 B. X. Zhang¹, D. H. Zhang³⁹, G. Y. Zhang¹⁸, H. Zhang⁶⁶, H. H. Zhang⁵⁴, H. H. Zhang³⁰,
 H. Y. Zhang^{1,53}, J. J. Zhang⁴⁷, J. L. Zhang⁷², J. Q. Zhang³⁷, J. W. Zhang^{1,53,58}, J. X. Zhang^{34,j,k},
 J. Y. Zhang¹, J. Z. Zhang^{1,58}, Jianyu Zhang^{1,58}, Jiawei Zhang^{1,58}, L. M. Zhang⁵⁶, L. Q. Zhang⁵⁴,
 Lei Zhang³⁸, P. Zhang¹, Q. Y. Zhang^{35,75}, Shuihan Zhang^{1,58}, Shulei Zhang^{23,h}, X. D. Zhang⁴¹,
 X. M. Zhang¹, X. Y. Zhang⁵⁰, X. Y. Zhang⁴⁵, Y. Zhang⁶⁴, Y. T. Zhang⁷⁵, Y. H. Zhang^{1,53},
 Yan Zhang^{66,53}, Yao Zhang¹, Z. H. Zhang¹, Z. Y. Zhang⁷¹, Z. Y. Zhang³⁹, G. Zhao¹,
 J. Zhao³⁵, J. Y. Zhao^{1,58}, J. Z. Zhao^{1,53}, Lei Zhao^{66,53}, Ling Zhao¹, M. G. Zhao³⁹, Q. Zhao¹,
 S. J. Zhao⁷⁵, Y. B. Zhao^{1,53}, Y. X. Zhao^{28,58}, Z. G. Zhao^{66,53}, A. Zhemchugov^{32,a}, B. Zheng⁶⁷,
 J. P. Zheng^{1,53}, Y. H. Zheng⁵⁸, B. Zhong³⁷, C. Zhong⁶⁷, X. Zhong⁵⁴, H. Zhou⁴⁵, L. P. Zhou^{1,58},

X. Zhou⁷¹, X. K. Zhou⁵⁸, X. R. Zhou^{66,53}, X. Y. Zhou³⁵, Y. Z. Zhou^{10,f}, J. Zhu³⁹, K. Zhu¹, K. J. Zhu^{1,53,58}, L. X. Zhu⁵⁸, S. H. Zhu⁶⁵, S. Q. Zhu³⁸, W. J. Zhu^{10,f}, Y. C. Zhu^{66,53}, Z. A. Zhu^{1,58}, B. S. Zou¹, J. H. Zou¹

¹ *Institute of High Energy Physics, Beijing 100049, People's Republic of China*

² *Beihang University, Beijing 100191, People's Republic of China*

³ *Beijing Institute of Petrochemical Technology, Beijing 102617, People's Republic of China*

⁴ *Bochum Ruhr-University, D-44780 Bochum, Germany*

⁵ *Carnegie Mellon University, Pittsburgh, Pennsylvania 15213, USA*

⁶ *Central China Normal University, Wuhan 430079, People's Republic of China*

⁷ *Central South University, Changsha 410083, People's Republic of China*

⁸ *China Center of Advanced Science and Technology, Beijing 100190, People's Republic of China*

⁹ *COMSATS University Islamabad, Lahore Campus, Defence Road, Off Raiwind Road, 54000 Lahore, Pakistan*

¹⁰ *Fudan University, Shanghai 200433, People's Republic of China*

¹¹ *G.I. Budker Institute of Nuclear Physics SB RAS (BINP), Novosibirsk 630090, Russia*

¹² *GSI Helmholtzcentre for Heavy Ion Research GmbH, D-64291 Darmstadt, Germany*

¹³ *Guangxi Normal University, Guilin 541004, People's Republic of China*

¹⁴ *Guangxi University, Nanning 530004, People's Republic of China*

¹⁵ *Hangzhou Normal University, Hangzhou 310036, People's Republic of China*

¹⁶ *Hebei University, Baoding 071002, People's Republic of China*

¹⁷ *Helmholtz Institute Mainz, Staudinger Weg 18, D-55099 Mainz, Germany*

¹⁸ *Henan Normal University, Xinxiang 453007, People's Republic of China*

¹⁹ *Henan University of Science and Technology, Luoyang 471003, People's Republic of China*

²⁰ *Henan University of Technology, Zhengzhou 450001, People's Republic of China*

²¹ *Huangshan College, Huangshan 245000, People's Republic of China*

²² *Hunan Normal University, Changsha 410081, People's Republic of China*

²³ *Hunan University, Changsha 410082, People's Republic of China*

²⁴ *Indian Institute of Technology Madras, Chennai 600036, India*

²⁵ *Indiana University, Bloomington, Indiana 47405, USA*

²⁶ *INFN Laboratori Nazionali di Frascati , (A)INFN Laboratori Nazionali di Frascati, I-00044, Frascati, Italy; (B)INFN Sezione di Perugia, I-06100, Perugia, Italy; (C)University of Perugia, I-06100, Perugia, Italy*

²⁷ *INFN Sezione di Ferrara, (A)INFN Sezione di Ferrara, I-44122, Ferrara, Italy; (B)University of Ferrara, I-44122, Ferrara, Italy*

²⁸ *Institute of Modern Physics, Lanzhou 730000, People's Republic of China*

²⁹ *Institute of Physics and Technology, Peace Avenue 54B, Ulaanbaatar 13330, Mongolia*

³⁰ *Jilin University, Changchun 130012, People's Republic of China*

³¹ *Johannes Gutenberg University of Mainz, Johann-Joachim-Becher-Weg 45, D-55099 Mainz, Germany*

³² *Joint Institute for Nuclear Research, 141980 Dubna, Moscow region, Russia*

- ³³ *Justus-Liebig-Universitaet Giessen, II. Physikalisches Institut, Heinrich-Buff-Ring 16, D-35392 Giessen, Germany*
- ³⁴ *Lanzhou University, Lanzhou 730000, People's Republic of China*
- ³⁵ *Liaoning Normal University, Dalian 116029, People's Republic of China*
- ³⁶ *Liaoning University, Shenyang 110036, People's Republic of China*
- ³⁷ *Nanjing Normal University, Nanjing 210023, People's Republic of China*
- ³⁸ *Nanjing University, Nanjing 210093, People's Republic of China*
- ³⁹ *Nankai University, Tianjin 300071, People's Republic of China*
- ⁴⁰ *National Centre for Nuclear Research, Warsaw 02-093, Poland*
- ⁴¹ *North China Electric Power University, Beijing 102206, People's Republic of China*
- ⁴² *Peking University, Beijing 100871, People's Republic of China*
- ⁴³ *Qufu Normal University, Qufu 273165, People's Republic of China*
- ⁴⁴ *Shandong Normal University, Jinan 250014, People's Republic of China*
- ⁴⁵ *Shandong University, Jinan 250100, People's Republic of China*
- ⁴⁶ *Shanghai Jiao Tong University, Shanghai 200240, People's Republic of China*
- ⁴⁷ *Shanxi Normal University, Linfen 041004, People's Republic of China*
- ⁴⁸ *Shanxi University, Taiyuan 030006, People's Republic of China*
- ⁴⁹ *Sichuan University, Chengdu 610064, People's Republic of China*
- ⁵⁰ *Soochow University, Suzhou 215006, People's Republic of China*
- ⁵¹ *South China Normal University, Guangzhou 510006, People's Republic of China*
- ⁵² *Southeast University, Nanjing 211100, People's Republic of China*
- ⁵³ *State Key Laboratory of Particle Detection and Electronics, Beijing 100049, Hefei 230026, People's Republic of China*
- ⁵⁴ *Sun Yat-Sen University, Guangzhou 510275, People's Republic of China*
- ⁵⁵ *Suranaree University of Technology, University Avenue 111, Nakhon Ratchasima 30000, Thailand*
- ⁵⁶ *Tsinghua University, Beijing 100084, People's Republic of China*
- ⁵⁷ *Turkish Accelerator Center Particle Factory Group, (A)Istinye University, 34010, Istanbul, Turkey; (B)Near East University, Nicosia, North Cyprus, Mersin 10, Turkey*
- ⁵⁸ *University of Chinese Academy of Sciences, Beijing 100049, People's Republic of China*
- ⁵⁹ *University of Groningen, NL-9747 AA Groningen, The Netherlands*
- ⁶⁰ *University of Hawaii, Honolulu, Hawaii 96822, USA*
- ⁶¹ *University of Jinan, Jinan 250022, People's Republic of China*
- ⁶² *University of Manchester, Oxford Road, Manchester, M13 9PL, United Kingdom*
- ⁶³ *University of Muenster, Wilhelm-Klemm-Strasse 9, 48149 Muenster, Germany*
- ⁶⁴ *University of Oxford, Keble Road, Oxford OX13RH, United Kingdom*
- ⁶⁵ *University of Science and Technology Liaoning, Anshan 114051, People's Republic of China*
- ⁶⁶ *University of Science and Technology of China, Hefei 230026, People's Republic of China*
- ⁶⁷ *University of South China, Hengyang 421001, People's Republic of China*
- ⁶⁸ *University of the Punjab, Lahore-54590, Pakistan*
- ⁶⁹ *University of Turin and INFN, (A)University of Turin, I-10125, Turin, Italy; (B)University of Eastern Piedmont, I-15121, Alessandria, Italy; (C)INFN, I-10125, Turin, Italy*

- ⁷⁰ *Uppsala University, Box 516, SE-75120 Uppsala, Sweden*
- ⁷¹ *Wuhan University, Wuhan 430072, People's Republic of China*
- ⁷² *Xinyang Normal University, Xinyang 464000, People's Republic of China*
- ⁷³ *Yunnan University, Kunming 650500, People's Republic of China*
- ⁷⁴ *Zhejiang University, Hangzhou 310027, People's Republic of China*
- ⁷⁵ *Zhengzhou University, Zhengzhou 450001, People's Republic of China*
- ^a *Also at the Moscow Institute of Physics and Technology, Moscow 141700, Russia*
- ^b *Also at the Novosibirsk State University, Novosibirsk, 630090, Russia*
- ^c *Also at the NRC "Kurchatov Institute", PNPI, 188300, Gatchina, Russia*
- ^d *Also at Goethe University Frankfurt, 60323 Frankfurt am Main, Germany*
- ^e *Also at Key Laboratory for Particle Physics, Astrophysics and Cosmology, Ministry of Education; Shanghai Key Laboratory for Particle Physics and Cosmology; Institute of Nuclear and Particle Physics, Shanghai 200240, People's Republic of China*
- ^f *Also at Key Laboratory of Nuclear Physics and Ion-beam Application (MOE) and Institute of Modern Physics, Fudan University, Shanghai 200443, People's Republic of China*
- ^g *Also at State Key Laboratory of Nuclear Physics and Technology, Peking University, Beijing 100871, People's Republic of China*
- ^h *Also at School of Physics and Electronics, Hunan University, Changsha 410082, China*
- ⁱ *Also at Guangdong Provincial Key Laboratory of Nuclear Science, Institute of Quantum Matter, South China Normal University, Guangzhou 510006, China*
- ^j *Also at Frontiers Science Center for Rare Isotopes, Lanzhou University, Lanzhou 730000, People's Republic of China*
- ^k *Also at Lanzhou Center for Theoretical Physics, Lanzhou University, Lanzhou 730000, People's Republic of China*
- ^l *Also at the Department of Mathematical Sciences, IBA, Karachi , Pakistan*